Validation of a Genetic-Algorithm-Optimized Coplanar Stripline Filter Using HFSS and ABCD Matrix Modeling

by

Tannaz Asadi Shad

BSC, Shahid Beheshti University, 2017

MSC, Shahid Beheshti University, 2019

A Project Submitted in Partial Fulfillment of the Requirements for the Degree of

MASTER OF ENGINEERING

in the Department of Electrical and Computer Engineering

We acknowledge and respect the Lək̓ʷəŋən (Songhees and Esquimalt) Peoples on whose territory the university stands, and the Lək̓ʷəŋən and W̱SÁNEĆ Peoples whose historical relationships with the land continue to this day.

University of Victoria

Validation of a Genetic-Algorithm-Optimized Coplanar Stripline Filter Using HFSS and ABCD Matrix Modeling

by

Tannaz Asadi Shad

BSC, Shahid Beheshti University, 2013

MSC, Shahid Beheshti University, 2019

Dr. Levi Smith, Supervisor

(Department of Electrical and Computer Engineering)

Supervisory Committee

Dr. Tao Lu

Abstract

This work presents a hybrid design framework for terahertz (THz) filters that integrates genetic algorithm (GA) optimization with ABCD matrix modeling and full-wave validation using HFSS. The proposed approach enables efficient inverse design by combining fast circuit-level analysis with electromagnetic accuracy.

The developed framework, based on the work of Ali Dehghanian (2025) [32], employs a GA to explore a binary design space representing metallic and dielectric pixel distributions. Each candidate geometry is evaluated using an analytical ABCD model, enabling rapid calculation of S-parameters during optimization. The final geometry is then validated through finite-element simulation in HFSS to ensure physical accuracy. Two filter types were designed and evaluated: a low-pass filter (LPF) and a band-stop filter (BSF), with performance analyzed across frequencies ranging from 0.25 THz to 2.0 THz. For the LPF, the results show that at lower frequencies (0.25 THz), the design achieved strong attenuation (–10.2 dB) but required higher structural complexity and slower convergence. As the frequency increased, the optimization became more stable and efficient, with consistent convergence behavior and improved transmission characteristics. At higher frequencies (1.5–2.0 THz), the LPF demonstrated faster convergence, reduced structural complexity (as low as 12 rows), and stable performance with fitness values around –6.3 dB.

For the BSF, a similar trend was observed. Lower frequencies exhibited wider stopbands but slower convergence, while mid-range frequencies (0.75–1.0 THz) showed improved stability and faster convergence. At higher frequencies, the BSF achieved stronger notch characteristics and more efficient optimization, with the best performance observed at 2.0 THz (–4.844 dB), along with smooth convergence and reduced parameter sensitivity.

Across both filter types, the results indicate that increasing frequency leads to improved optimization efficiency, reduced structural requirements, and more stable convergence behavior. A comparison between ABCD-based analytical results and HFSS simulations shows strong agreement in both magnitude and phase responses, validating the accuracy and reliability of the proposed GA–ABCD–HFSS framework.

Overall, the proposed methodology provides a fast, consistent, and physically reliable approach for designing high-performance THz filters.

Contents

List of Tables

List of Figures

Acronyms

Au Gold

CPS Coplanar Strip

CPW Coplanar Waveguide

DC Direct Current

FDTD Finite-Difference Time-Domain

FEM Finite Element Method

GA Genetic Algorithm

GaAs Gallium Arsenide

GHz Gigahertz

LPF Low-Pass Filter

PCS Photoconductive Switch

RMSE Root Mean Squared Error

SRR split-ring resonator

TEM Transverse Electro-Magnetic

THz Terahertz

TSoC Terahertz System-on-Chip

UV Ultraviolet

Acknowledgements

I would like to express my deepest gratitude to Dr. Levi Smith, my supervisor, for his invaluable guidance, encouragement, and insight throughout this project. His expertise, patience, and thoughtful feedback were instrumental in shaping both the technical and conceptual direction of my work.

I would also like to extend my appreciation to Ali Dehghanian, whose doctoral research and mentorship provided an essential foundation for this project. His work and advice greatly guides me and deepened my understanding of terahertz filter design.

Finally, I am grateful to my family, colleagues, and friends for their encouragement and kindness, which made this journey both meaningful and fulfilling.

Dedication

To my dear parents, whose endless love, patience, and faith have been the foundation of all that I am. And to my husband, Philip — my constant source of strength, laughter, and calm through every challenge. His unwavering support and belief in me have made this journey possible.

1. Introduction

1.1. THz wave and its application

Terahertz (THz) electromagnetic waves have attracted considerable scientific interest due to their distinctive physical properties and potential applications across communication, sensing, and imaging technologies. This frequency range, which spans approximately 0.1–10 THz is depicted in Figure 1, bridges the gap between electronics and photonics—often referred to as the THz gap—and has attracted growing attention due to its vast scientific and technological potential [1]. The energy of THz photons is relatively low—about 4.14 meV at 1 THz—making this radiation non-ionizing and therefore safe for biomedical and material-imaging applications, unlike higher-energy X-rays [2].

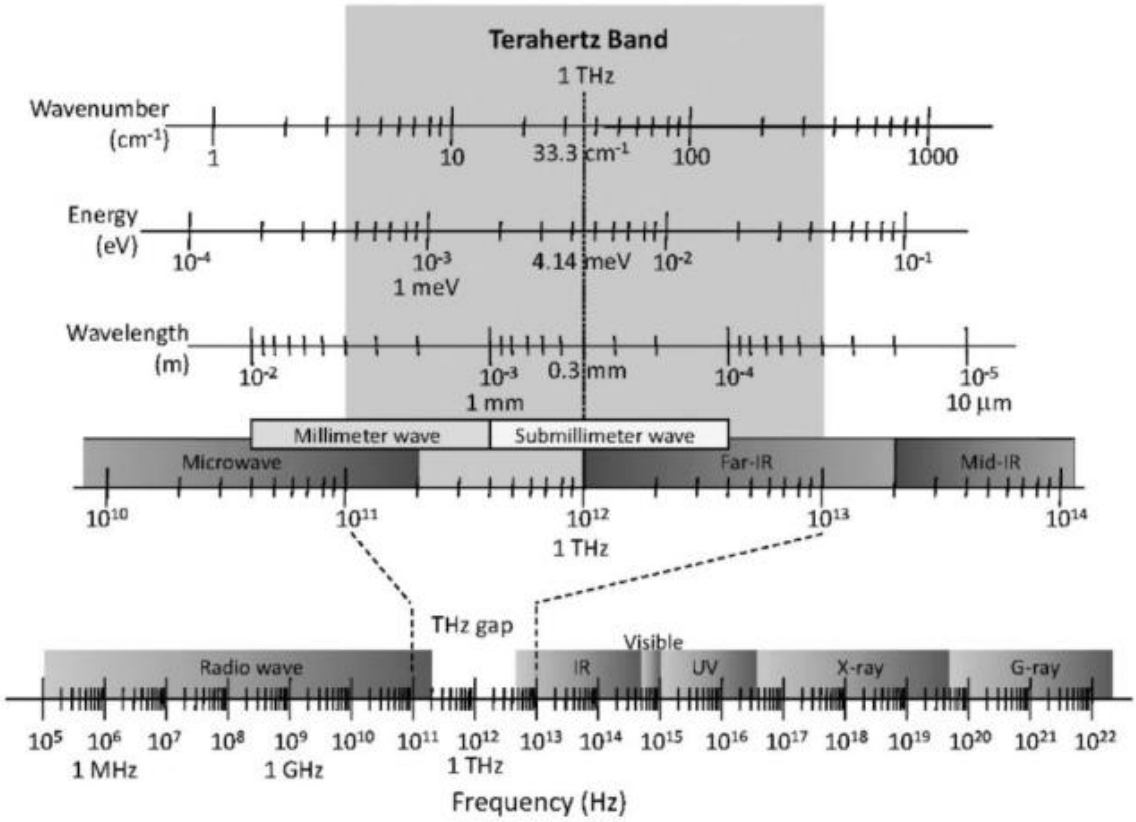

Figure 1 Terahertz band in electromagnetic spectrum [3]

The THz band's unique characteristics—such as its ability to penetrate nonmetallic materials, sensitivity to molecular vibrations, and broad available bandwidth—make it highly valuable for diverse applications in imaging, spectroscopy, communications, and sensing. For example, THz waves can pass through clothing, plastics, ceramics, and biological tissues without causing damage, enabling non-invasive imaging and security screening. Jepsen et al. [4] demonstrated the effectiveness of THz radiation in biomedical imaging, while Peiponen et al. [5] and Yang et al. [6] explored its applications in material and tissue characterization.

In parallel with these developments, advances in femtosecond laser systems, photoconductive antennas, and nonlinear optical materials have made THz generation and detection increasingly accessible [7]. Despite these achievements, widespread implementation of THz technology still faces persistent challenges—particularly in the efficient generation, sensitive detection, and compact system integration of THz components [7], [8]. These challenges have motivated significant research into THz system-on-chip (TSoC) architectures, where planar transmission lines and integrated filters can manipulate and guide THz signals effectively.

One of the most promising areas for THz deployment lies in high-speed wireless communication. The immense bandwidth available in the THz range supports terabit-per-second data rates, positioning it as a potential foundation for 6G and beyond. Studies by Kleine et al. [9], and Tekbiyik et al. [10] have outlined the potential of THz-based networks for short-range ultrafast communication, data backhaul, and high-capacity links. As such, the THz region not only serves as a fertile ground for experimental science but also as a frontier for emerging communication and sensing technologies.

The terahertz domain combines the best features of electronic and optical systems—large bandwidths, molecular sensitivity, and non-ionizing radiation—while presenting unique design challenges. The continued evolution of THz sources, detectors, and integrated components is paving the way for compact, efficient, and scalable systems that could redefine future applications in communications, sensing, and imaging.

1.2. THz Field Guiding Technologies

Guiding electromagnetic waves at terahertz (THz) frequencies presents unique challenges. While the principles of microwave transmission lines apply, losses, dispersion, and fabrication tolerances

become increasingly critical as wavelengths shrink to tens or hundreds of micrometers. Achieving low-loss, broadband, and easily manufacturable guiding structures has therefore been one of the major engineering obstacles in the development of compact THz systems. Among several available options—such as microstrip, coplanar waveguide (CPW), and coplanar stripline (CPS)—the CPS structure stands out because of its elegant simplicity, planar geometry, and excellent compatibility with integrated fabrication techniques [11], [12]. When fabricated on thin dielectric membranes, CPS structures exhibit minimal attenuation and dispersion, making them ideal for terahertz system-on-chip (TSoC) applications that integrate sources, filters, and detectors on a single platform.

1.2.1 Coplanar Strip Transmission Line and Coplanar Waveguide

A coplanar stripline (CPS) consists of two parallel metallic conductors placed on the same dielectric substrate, separated by a gap, S, and having a width, W. Because both conductors reside on the same plane, CPS eliminates the need for a ground plane—one of the key differences from the microstrip configuration. This planar structure provides several advantages: it avoids vertical vias, simplifies fabrication, and enables seamless integration with balanced components such as differential amplifiers, dipole antennas, and optical photoconductive switches [13].

The CPS supports a quasi-transverse electromagnetic (quasi-TEM) mode in which equal and opposite currents flow on the two conductors. This results in a balanced field distribution with electric field lines confined primarily between the strips. Such a mode exhibits strong immunity to external noise and minimizes radiation, both of which are crucial for THz applications where the wavelengths are extremely small and the coupling to unwanted modes can easily degrade performance [14].

In contrast, the coplanar waveguide (CPW)—another widely used planar structure—features a central signal conductor bordered by two ground planes. Although CPW offers convenient probe access and straightforward integration with unbalanced circuits, it introduces higher parasitic capacitance to ground and typically suffers from greater dispersion at THz frequencies [15]. For these reasons, CPS has emerged as the preferred guiding structure for broadband THz components such as sensors, filters, and delay lines. Figure 2 illustrates the geometries of the coplanar stripline (CPS) and coplanar waveguide (CPW).

From a practical perspective, CPS lines are also attractive because their geometry is scalable. As frequencies rise into the THz regime, dimensions can be reduced proportionally without significantly changing impedance. When fabricated on ultrathin substrates—often silicon nitride (Si_3N_4) membranes less than 2 µm thick—the majority of the electromagnetic field propagates in air rather than in the dielectric, reducing loss and phase distortion. These properties make CPS the backbone of many recently developed on-chip THz measurement systems [16].

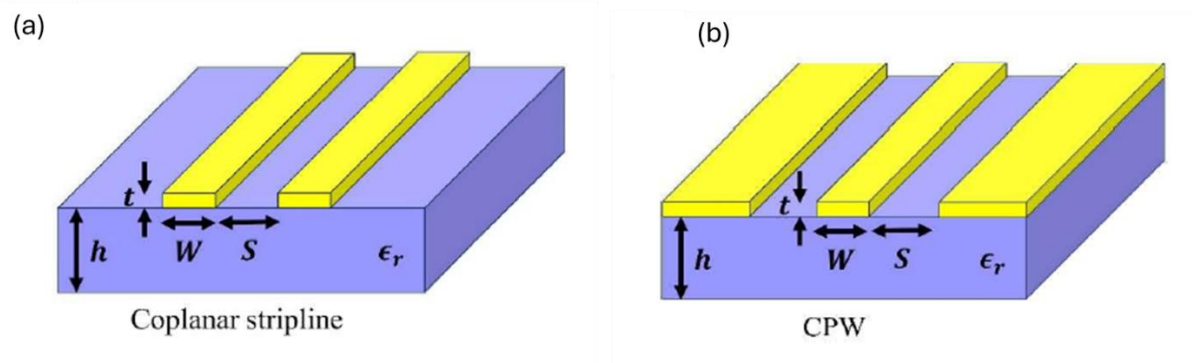

Figure 2 Cross-sectional illustration of two types of planar transmission lines fabricated on a substrate with dielectric constant εr. (a) coplanar strip lines, (b) coplanar waveguides [12]

1.2.2 Attenuation in Coplanar Strip lines

Even with their advantages, CPS lines are not lossless. As with any transmission medium, several physical mechanisms contribute to attenuation, and at THz frequencies these effects are amplified. The three dominant sources of loss are ohmic (conductor) loss, dielectric loss, and radiation loss.

1. Ohmic Loss:

At high frequencies, current in a conductor is confined to a thin surface layer, characterized by the skin depth, given by

$$\delta = \sqrt{\frac{2}{\omega\mu\sigma}} \qquad (1.1)$$

where ω is the angular frequency, µ the permeability, and σ the electrical conductivity of the metal [17]. As frequency increases, δ decreases, meaning that current flows through an ever-thinner region, increasing the effective resistance. Consequently, the surface resistance increases proportionally to the square root of frequency, causing higher insertion loss. In practice, additional

loss stems from fabrication imperfections such as surface roughness or thin metal films, which further elevate resistivity.

$$R_s = {}^{1}/_{\sigma\delta} \quad (1.2)$$

2. Dielectric Loss:

Dielectric attenuation arises from polarization processes within the substrate material. At THz frequencies, the rapidly oscillating electric field excites molecular vibrations in dielectric materials. In this work, silicon nitride (Si_3N_4) is used as the substrate due to its low loss characteristics at THz frequencies.

$$\varepsilon(\omega) = \varepsilon'(\omega) - j\varepsilon''(\omega) \quad (1.3)$$

Here, ε′(ω) denotes the real component of the permittivity, which governs the propagation of electromagnetic waves, while ε′′(ω) represents the imaginary component responsible for energy absorption within the material.

The dielectric loss is typically characterized by the loss tangent, expressed as:

$$\tan\delta_e = \frac{\varepsilon''(\omega)}{\varepsilon'(\omega)} \quad (1.4)$$

For Si_3N_4 at THz frequencies, the loss tangent is approximately $\tan\delta_e = 0.00526$, indicating relatively low dielectric loss. The loss tangent typically grows with frequency, meaning dielectric loss becomes a dominant factor in bulk substrates. To mitigate this, CPS lines are often fabricated on thin, low-permittivity membranes made of Si_3N_4, parylene, or polymers like polyimide. These materials limit dielectric absorption and confine most of the energy in the surrounding air.

3. Radiation Loss:

Radiation loss occurs when electromagnetic energy leaks from the guided mode into substrate modes or free space. This leakage is particularly pronounced when the substrate thickness approaches the wavelength or when there is a mismatch between the effective permittivity of the CPS mode and that of the substrate. For thick substrates, the guided mode travels faster above the substrate than within it, generating leaky waves that propagate into the dielectric at an angle determined by the permittivity ratio [18].

$$\alpha_{rad}^{CPS} = \pi^5 \left(\frac{3-\sqrt{8}}{2}\right) \sqrt{\frac{\varepsilon_{eff}(f)}{\varepsilon_r}} \left(1 - \frac{\varepsilon_{eff}(f)}{\varepsilon_r}\right)^2 \frac{(S+2W)^2 \varepsilon_r^{3/2}}{c^3 K'(k) K(k)} f^3 \quad (1.5)$$

In this expression, $\varepsilon_{eff}(f)$ refers to the frequency-dependent effective relative permittivity, ε_r denotes the substrate's relative permittivity, and c represents the speed of light in free space.

Two strategies are commonly used to mitigate this effect. First, reducing the stripline dimensions—the conductor width (W) and spacing (S)—can help confine the fields and lower radiation losses. However, this approach increases the line's resistance and conductor loss due to a smaller conduction area, making it less practical for scalable terahertz system-on-chip (TSoC) designs [11].

Reducing the substrate thickness also shifts surface-wave resonances to much higher frequencies—for instance, a 1 μm layer corresponds to a resonance near 54.3 THz—well beyond the operational range of interest. Consequently, ultra-thin membranes provide strong field confinement and significantly lower radiation losses, making them highly suitable for high-frequency THz integrated circuits [15].

4. Conductor Loss:

One of the dominant attenuation mechanisms in planar terahertz (THz) transmission lines is conductor loss, which arises from the finite electrical conductivity (σ) of the metallic traces forming the waveguide. When an electromagnetic wave propagates along a conductor, a portion of its energy is dissipated as heat due to the resistive nature of the metal. This phenomenon becomes increasingly significant at THz frequencies, where the skin effect confines current flow to a thin surface layer of the conductor, effectively increasing resistance [11], [14].

The attenuation coefficient due to conductor loss, denoted α_c, is expressed as:

$$\alpha_c \propto \frac{R_S(\omega)}{Z_0(\omega)} \quad (1.6)$$

where $Z_0(\omega)$ is the characteristic impedance of the transmission line, and $R_s(\omega)$ is the surface resistance of the conductor, given by:

$$R_s(\omega) = \sqrt{\frac{\pi f \mu(\omega)}{\sigma}} \quad (1.7)$$

The skin depth δ_s determines how deeply the current penetrates the conductor and is expressed as:

$$\delta_s = \sqrt{\frac{2}{\omega \mu(\omega) \sigma}} \quad (1.8)$$

At higher frequencies, the skin depth decreases, forcing current to flow closer to the surface and effectively increasing resistance. Since $R_s \propto \sqrt{f}$, conductor loss rises with frequency and decreases with higher conductivity.

In this study, gold (Au) was used as the conducting material, with an assumed conductivity of σ_{Au}=4.1×107 S/m, consistent with reported THz device simulations [15]. Materials with higher conductivity or smoother surfaces can significantly reduce ohmic losses and improve overall device performance.

1.2.3. Dispersion in Coplanar Striplines

Dispersion describes how the phase velocity of a signal varies with frequency. In a dispersive medium, different frequency components travel at different speeds, causing a short pulse to broaden as it propagates. This phenomenon becomes especially significant for THz pulses, which are inherently broadband and often used in time-domain spectroscopy or ultrafast communication systems [19].

In CPS structures, both material dispersion and modal dispersion can be present. In a CPS fabricated on a thick substrate, the guided field penetrates deeply into the dielectric, and the frequency-dependent permittivity of the material introduces dispersion. Additionally, modal dispersion may arise due to the distribution of electromagnetic fields between air and substrate regions. As a result, the phase and group velocities of different frequency components become unequal, leading to temporal broadening and signal distortion[12].

Thin-membrane CPS structures mitigate this problem by confining most of the field in air, where the permittivity is constant and frequency-independent. As a result, the effective permittivity ε_{eff} of the line remains nearly constant across a wide spectral range. Experimental observations have

shown that the phase velocity v_p of THz pulses in such lines is approximately 0.9 c' and remains stable up to several terahertz [20].

This low-dispersion behavior is a key enabler for many THz applications. In THz time-domain spectroscopy (THz-TDS), preserving the temporal shape of a pulse allows precise extraction of material parameters such as refractive index and absorption coefficient. In high-speed communication links, low dispersion ensures data integrity by preventing inter-symbol interference. These advantages have made CPS transmission lines essential components in the emerging field of THz integrated photonics [15].

1.3. THz Filters

Filtering is one of the most essential operations in any electromagnetic system. Whether in low-frequency electronics or at the terahertz (THz) frontier, filters are responsible for selecting, shaping, and refining spectral components to achieve the desired signal performance. In the THz domain, filters play an especially critical role: they determine bandwidth, control noise, and enable precision in both sensing and communication applications [14].

The development of THz filters mirrors the broader evolution of electromagnetic design—from classical lumped-element networks to distributed and metamaterial-inspired architectures. Conventional filters are built from capacitors and inductors that define cutoff frequencies and resonance behaviors. At THz frequencies, however, physical dimensions become comparable to the wavelength, and the discrete components of traditional circuits are replaced by distributed transmission-line segments, periodic resonant structures, or metamaterial inclusions such as split-ring resonators (SRRs).

These new approaches have opened up the possibility of building compact, high-performance, and even tunable THz filters that can be integrated on-chip using planar fabrication techniques [12], [15].

1.3.1. Fundamentals of Filter Types

Filters are generally categorized based on the portion of the spectrum they allow or reject: low-pass, high-pass, band-pass, and band-stop. Each type manipulates the spectral content of signals

differently, and their characteristics can be realized through various topologies or resonant configurations.

(a) Low-Pass Filters

Low-pass filters permit low-frequency components to pass while attenuating higher frequencies. They are widely used to suppress high-frequency noise or harmonics. In traditional lumped-element form, a low-pass filter may consist of series inductors and shunt capacitors arranged to achieve the desired roll-off characteristics [11]. In the distributed domain, a transmission-line low-pass filter uses shorted stubs or stepped-impedance sections that mimic the same function. In Figure 3 the cutoff frequency fc marks the point where the magnitude of transmission |S21| drops by 3 dB.

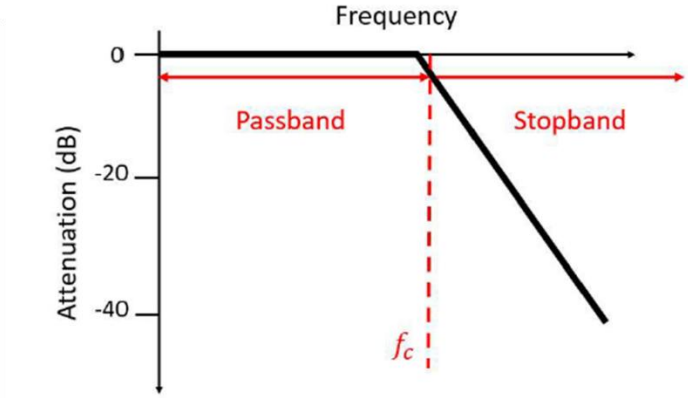

Figure 3 Low pass Filter [12]

(b) High-Pass Filters

Conversely, high-pass filters show in Figure 4 block low frequencies while allowing higher frequencies to pass. The simplest implementation in lumped circuits swaps the positions of inductors and capacitors compared to the low-pass configuration. In planar THz systems, high-pass behavior can be achieved by etching capacitive gaps or slots that block DC and low-frequency currents while allowing higher-frequency fields to couple across the discontinuity [15].

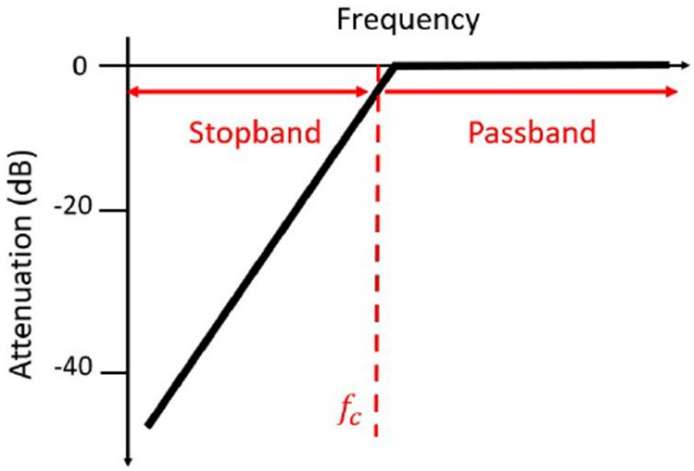

Figure 4 . High pass filter, frequency response [12]

(c) Band-Pass Filters

Band-pass filters depict in Figure 5 transmit only a specific frequency band between two cutoff points f_{c1} and f_{ch} . At THz frequencies, these filters are often realized using resonant cavities, coupled microstrip or coplanar waveguide sections, or periodically loaded structures that form passbands due to constructive interference. For instance, a periodic array of SRRs or complementary SRRs (CSRRs) can be used to form a metamaterial band-pass filter, where each unit cell resonates at a specific frequency and the entire lattice supports transmission only around that resonance [18]. Band-pass filters are crucial in THz spectroscopy and imaging, where narrow spectral selectivity allows differentiation between chemical signatures.

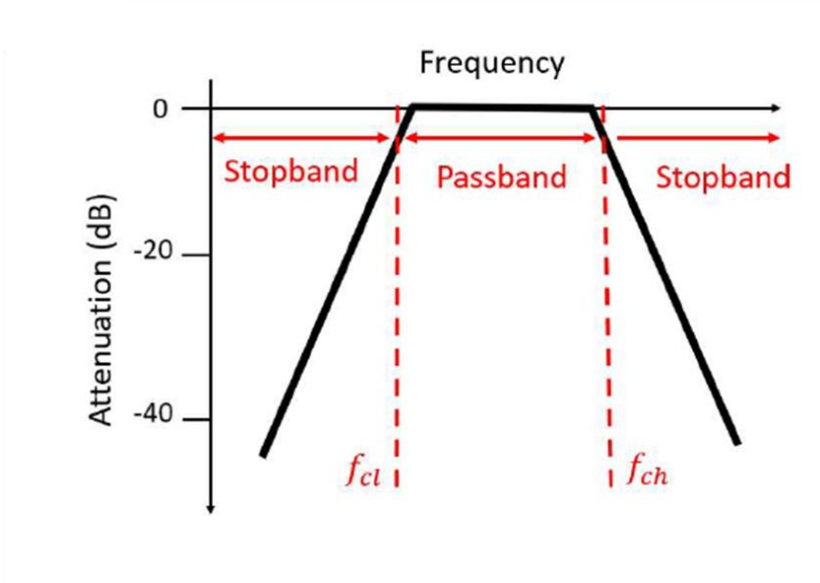

Figure 5 Passband filter, General frequency response [12]

(d) Band-Stop (Notch) Filters

Band-stop or notch filters in Figure 6 operate in the opposite way—they reject a narrow range of frequencies while passing those below and above it. The simplest notch filters consist of parallel LC resonant tanks that create a sharp dip in transmission at the resonance frequency.

$$f_0 = \frac{1}{2\pi\sqrt{LC}} \qquad (1.6)$$

At THz frequencies, these filters are often implemented using sub-wavelength resonant structures, such as split-ring resonators (SRRs), which naturally exhibit a band-stop response due to their magnetic resonance [21]. Asadi's work [12] demonstrated a practical THz band-stop filter by integrating varying-radius SRRs between the conductors of a coplanar stripline (CPS). The resulting device achieved a measured center frequency of 1.06 THz and a −3 dB bandwidth of 0.36 THz, confirming the strong filtering effect and agreement between simulation and experimental data.

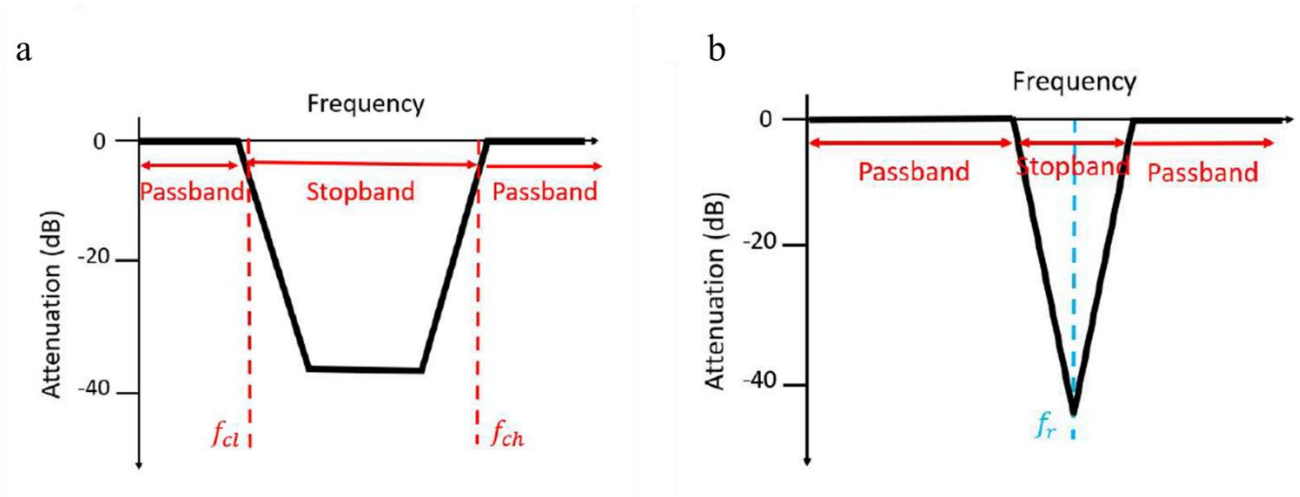

Figure 6 . a. Band stop filter, b. notch band stop filter [12]

1.3.2. Phase and Frequency Response

The amplitude response of a filter determines which frequencies are transmitted or rejected, but the phase response dictates how different spectral components are delayed as they pass through. In high-speed communication or time-domain spectroscopy, maintaining a linear phase response within the passband is vital because nonlinear phase shifts cause pulse distortion and timing errors [22].

For a linear phase filter, the relationship between input and output is simply a delayed version of the same waveform. However, when the phase is nonlinear, higher and lower frequency components experience different time delays, leading to waveform broadening. This is especially problematic in THz systems that rely on femtosecond pulses. Hence, modern THz filter design often prioritizes both amplitude flatness and phase linearity, balancing insertion loss with minimal group-delay variation [23].

1.3.3. Periodic and Metamaterial-Based THz Filters

Moving beyond traditional designs, many THz filters now employ periodic and metamaterial-based architectures, which leverage resonant unit cells to manipulate wave propagation in unprecedented ways.

A periodic structure is composed of repeated elements along the transmission path—each acting as a small resonant or reactive section. These periodic inclusions can produce stopbands (frequency

regions of strong attenuation) or passbands (regions of enhanced transmission) depending on the geometry and coupling between cells [13].

In the idealized infinite periodic structure, the electromagnetic wave interacts with a lattice that extends indefinitely. This scenario can be analyzed using Bloch–Floquet theory, where the propagation constant β satisfies the periodic boundary condition

$$e^{j\beta p} = A + \frac{B}{Z_0} \tag{1.7}$$

where $p$represents the unit-cell length, $Z_0$is the characteristic impedance, A and $B$are elements of the unit-cell ABCD matrix [24]. The resulting dispersion diagram reveals allowed and forbidden frequency bands—regions where energy either propagates or is reflected due to Bragg resonance.

In real devices, structures are finite and terminated by loads or ports, introducing reflections and edge effects that slightly modify the theoretical stopband width. Dehghanian [15] explored these effects by constructing CPS filters composed of multiple GA-optimized unit cells. By cascading ABCD matrices of each cell, he demonstrated how practical filters exhibit predictable resonant dips corresponding to the designed stopbands, confirming good agreement between analytical models and full-wave HFSS simulations. The relationship between voltage and current at successive unit cells is expressed using the ABCD matrix formulation:

$$\begin{bmatrix} V_n \\ I_n \end{bmatrix} = \begin{bmatrix} A & B \\ C & D \end{bmatrix} \cdot \begin{bmatrix} V_{n+1} \\ I_{n+1} \end{bmatrix} \tag{1.8}$$

where $V_n$and $I_n$represent the voltage and current at the input of the n-th unit cell, and V_{n+1}, I_{n+1}correspond to the output. The ABCD matrix characterizes how each unit cell transforms the electrical signals, allowing multiple cells to be cascaded by simple matrix multiplication. This provides an efficient way to model the overall behavior of periodic filter structures and predict their transmission and reflection characteristics.

These metamaterial-inspired periodic filters provide unparalleled miniaturization and performance tunability. By adjusting geometric parameters such as the width, spacing, and number of unit cells, designers can tailor the bandwidth, rejection depth, and phase characteristics without relying on bulky external components.

1.3.4. Design Evolution and Applications

The ongoing evolution of THz filters reflects a convergence of classical circuit theory and modern computational design. Techniques such as genetic algorithms (GAs) and machine-learning-driven optimization are now applied to automate the inverse design of complex geometries. Dehghanian's GA-based optimization, for example, encoded each CPS section as a pixelated gold-air map and used an ABCD-matrix surrogate model to rapidly compute transmission responses during optimization. Once the design converged, a full-wave simulation validated the final structure with near-perfect correlation below 0.9 THz [15].

Such computationally guided methods accelerate the design cycle and enable the discovery of unconventional geometries that outperform traditional periodic filters. Applications range from selective molecular sensing, where narrowband filters isolate vibrational modes, to THz communications, where broadband filters define channel bandwidths with sub-picosecond group delays.

Ultimately, as THz technology matures, filter design continues to serve as a critical bridge—linking theoretical electromagnetic modeling with practical integrated devices capable of operating in one of the most challenging yet promising regions of the spectrum. These analytical and computational insights form the foundation for the inverse-design framework discussed in Chapter 2.

2. Inverse Design Methodology for THz Filters

The design of terahertz (THz) filters has traditionally relied on well-established microwave engineering methods, where the geometry of a device—such as stubs, resonators, or transmission lines—is defined analytically and refined through parameter tuning. While these conventional methods remain valuable, they become increasingly limited when applied to compact, high-performance THz systems that demand both miniaturization and nonintuitive field control [11]. Classical design strategies are often constrained by predefined topologies and cannot efficiently explore unconventional geometries or achieve fine spectral tuning within the subwavelength regime.

2.1. Evolution of Inverse Design

Inverse design originated in nanophotonics, where it has been used to develop photonic structures far beyond the reach of analytical models. In silicon photonics, for instance, inverse design has led to ultracompact wavelength filters, mode converters, and multiplexers, all with nonintuitive geometries that outperform their manually designed counterparts [25], [26]. These methods have proven particularly powerful in photonic integrated circuits (PICs), where device density, compactness, and precise spectral control are critical. As the field matured, inverse design became a central tool for nanophotonic device optimization, allowing for robust, multifunctional components with improved efficiency, reduced footprint, and complex field manipulation capabilities. The success of these techniques in the optical domain has inspired their adoption in terahertz engineering, where similar challenges—compactness, spectral precision, and fabrication constraints—are equally prominent [27]. In recent years, inverse-design techniques have transformed the development of nanophotonic and THz components including absorbers, antennas, and meta-surfaces [15]. Their success is attributed to two capabilities: (1) the use of efficient optimization algorithms—such as genetic algorithms (GAs), particle-swarm optimization, or neural-network surrogates—to explore high-dimensional design spaces; and (2) the integration of fast electromagnetic solvers or analytical surrogate models that evaluate candidate structures at low computational cost. These methods provide a pathway toward compact,

fabrication-ready THz filters integrated on coplanar stripline (CPS) or coplanar-waveguide (CPW) platforms compatible with standard lithography [29].

2.2. Foundations of Periodic Planar Terahertz Filter Design

This section outlines the fundamental principles underlying the periodic filter structures used in this work. Planar THz filters operate by introducing periodic variations in the characteristic impedance of a guided-wave transmission line. These periodic structures, implemented using CPS or CPW configurations, create frequency-selective behavior through constructive and destructive interference.

In particular, the proposed design framework is based on cascading unit cells with different impedance characteristics, forming a periodic structure. The performance of such filters—defined by center frequency, bandwidth, and rejection depth—is governed by the impedance contrast between adjacent sections and the spatial periodicity of the structure [29]. The central frequency of a periodic filter is approximately

$$f_c = \frac{c}{2\Lambda\sqrt{\varepsilon_{re}}}, \tag{2.1}$$

where c is the speed of light, Λ is the period, and ε_{re} is the effective relative permittivity obtained from full-wave simulations. The fractional bandwidth depends on the impedance contrast between adjacent sections [29]:

$$\frac{\Delta f}{f_c} = \frac{4}{\pi}\sin^{-1}\left(\frac{Z_0 - Z_1}{Z_0 + Z_1}\right) \tag{2.2}$$

where Z_0 and Z_1 denote the characteristic impedances. These relationships highlight the link between geometry and spectral response, forming the analytical foundation for inverse design.

At THz frequencies, full-wave analysis using the finite-element method (FEM) or finite-difference time-domain (FDTD) is computationally expensive. A more tractable analytical representation employs the ABCD-matrix formalism, in which each section of transmission line is modeled by a two-port matrix:

$$\begin{bmatrix} A & B \\ C & D \end{bmatrix} = \begin{bmatrix} \cos(\beta\Lambda) & jZ\sin(\beta\Lambda) \\ j\frac{1}{Z}\sin(\beta\Lambda) & \cos(\beta\Lambda) \end{bmatrix} \quad (2.3)$$

Cascading N sections yields the overall transfer matrix through simple multiplication. Scattering parameters are then derived as [29][15]:

$$S_{21} = \frac{2}{A+{}^{B}/_{Z_0}+CZ_0+D}, \quad S_{11} = \frac{A+{}^{B}/_{Z_0}-CZ_0+D}{A+{}^{B}/_{Z_0}+CZ_0+D} \quad (2.4)$$

where Z_0 is the reference impedance. This method captures the essential transmission characteristics of cascaded THz filters while avoiding repeated heavy FEM simulations, making it suitable for use as a surrogate model inside an optimization loop.

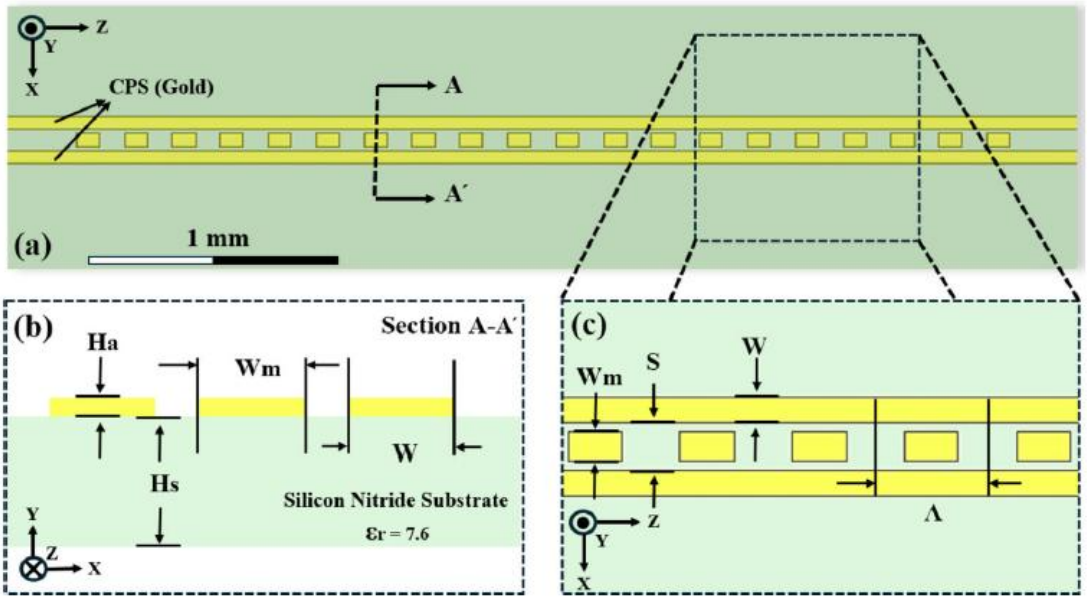

Figure 7 Schematic of the planar multimodal periodic terahertz filter based on alternating coplanar stripline (CPS) and coplanar waveguide (CPW) sections [29].

Figure 7 illustrates the physical configuration of the planar multimodal periodic terahertz filter used in this study. As shown in Fig. 7 (a), the structure consists of gold coplanar stripline (CPS) conductors patterned on a thin silicon-nitride (Si_3N_4) membrane substrate, forming alternating sections of CPS and coplanar waveguide (CPW) along the propagation direction (z-axis). The periodic modulation of these sections defines the stopband characteristics of the filter. The cross-section in Fig. 7 (b) shows the conductor thickness (H_a), substrate thickness (H_s), and the key

geometrical parameters: the central conductor width (W_m) and the outer conductor width (W). These dimensions determine the characteristic impedances of the CPW and CPS modes, respectively. The magnified top view in Fig. 7 (c) highlights a single unit cell of the periodic structure, with period (Λ) and spacing (S) between conductors. The alternating impedance profile generated by varying W_m and S enables control over the filter's center frequency and bandwidth. This configuration forms the foundation for the analytical ABCD-matrix modeling and the inverse-design optimization framework presented in subsequent sections.

2.3. Concept of Inverse Design

In an inverse-design framework, the designer specifies a target transfer function—for instance, the desired $S_{21}(f)$ magnitude and phase—and the algorithm searches for geometric parameters that minimize the discrepancy between simulated and target responses. The optimization variable vector may encode conductor widths, spacings, or even pixelized material distributions representing metal and dielectric regions. The fitness function quantifies agreement between simulated and target spectra. A common choice is the root-mean-square error (RMSE):

$$RMSE = \sqrt{\frac{1}{N}\sum_{i=1}^{N}(|S_{21}(f_i)| - |S_{21}^{target}(f_i)|)^2 + (|S_{11}(f_i)| - |S_{11}^{target}(f_i)|)^2} \qquad (2.5)$$

Weights can be introduced to emphasize particular frequency regions or phase linearity [15]. The optimization thus proceeds automatically without manual parameter sweeps, ensuring a direct link between performance goals and physical realization.

2.4. Genetic-Algorithm Optimization

The genetic algorithm (GA) is a stochastic evolutionary method inspired by natural selection [8]. It operates on a population of candidate solutions, each encoded as a chromosome that represents the structural parameters of the filter. The optimization begins with an initialization phase, where a random population of feasible designs is generated within the fabrication constraints. Each design is then evaluated by computing its ABCD-based S-parameters and determining a corresponding fitness value that reflects how closely the spectral response matches the target.

During the selection stage, individuals with higher fitness values are more likely to be chosen for reproduction, ensuring that favorable traits are propagated. The crossover operation combines segments from two parent chromosomes to produce offspring, enabling the exploration of new geometric configurations. To maintain diversity and prevent premature convergence, mutation introduces random perturbations to selected genes, such as changing conductor widths or toggling pixel states. Finally, elitism ensures that the best-performing individuals are directly carried over to the next generation, maintaining steady progress toward convergence [15]. These enhancements significantly improve the reliability of the GA-based inverse design process and enable the generation of robust, repeatable filter geometries that meet complex spectral requirements with high precision.

3. Genetic Algorithm–Based Inverse Design of a Low-Pass Terahertz Filter

This chapter presents the design, optimization, and validation of a Genetic-Algorithm (GA)–based inverse-design framework applied to a low-pass terahertz (THz) filter implemented on a coplanar stripline (CPS) structure. The method follows the optimization approach developed by Dehghanian et al. (2025) [35], where a GA searches for optimal metal–air pixel distributions that reproduce a desired frequency response. Each candidate geometry is rapidly evaluated using an analytical ABCD-matrix model, and the final structure is verified using full-wave finite-element simulation in ANSYS HFSS 2025.1. The goal of this chapter is to demonstrate how the GA–ABCD framework efficiently generates compact, non-intuitive low-pass geometries, validates the analytical model through comparison with HFSS, and evaluates the optimized device in terms of transmission, reflection, and phase response.

3.1. Design Objectives and Constraints

The design objectives in this work are based on the framework proposed by Ali Dehghanian [15], which targets the realization of a low-pass filter operating around 0.6 THz, with a 3-dB bandwidth of about 0.14 THz and a tunable rejection depth suitable for integration in terahertz systems. The device was required to maintain DC continuity for direct coupling to a photoconductive switch (PCS) source, ensure compatibility with planar lithographic fabrication, and preserve a fixed footprint of 300 µm × 2000 µm to facilitate integration within existing terahertz system-on-chip (TSoC) architectures. The designed structure consists of gold (Au) coplanar stripline (CPS) conductors with a conductivity of 2.16×10^7 S/m, chosen to model realistic conductor losses at THz frequencies, patterned on a thin silicon-nitride (Si_3N_4) membrane substrate of 1 µm thickness and relative permittivity of approximately $\varepsilon_{r,SiN} = 7.6$. Within this design, the optimization parameters correspond to the binary distribution of metallic and air pixels, which are spatially arranged in a discretized design domain to control the local characteristic impedance. The structural design variables were expressed as a binary matrix representing the spatial distribution of metallic and air pixels within the optimization region. Each pixel, with dimensions of 10 µm × 10 µm, defined the local impedance of the coplanar stripline section.

The optimization algorithm aimed to minimize the deviation between the target and simulated scattering parameters, ensuring that the resulting filter satisfied both spectral and fabrication constraints. Figure 8 shows the schematic of the GA-optimized planar THz filter, including the overall device layout, design parameters such as conductor width and spacing, and the cross-sectional view of the CPS structure patterned on a silicon-nitride substrate

This discretization allows the genetic algorithm to explore a wide range of geometrical configurations while satisfying fabrication and electrical continuity constraints, ultimately enabling precise spectral control of the filter response [32].

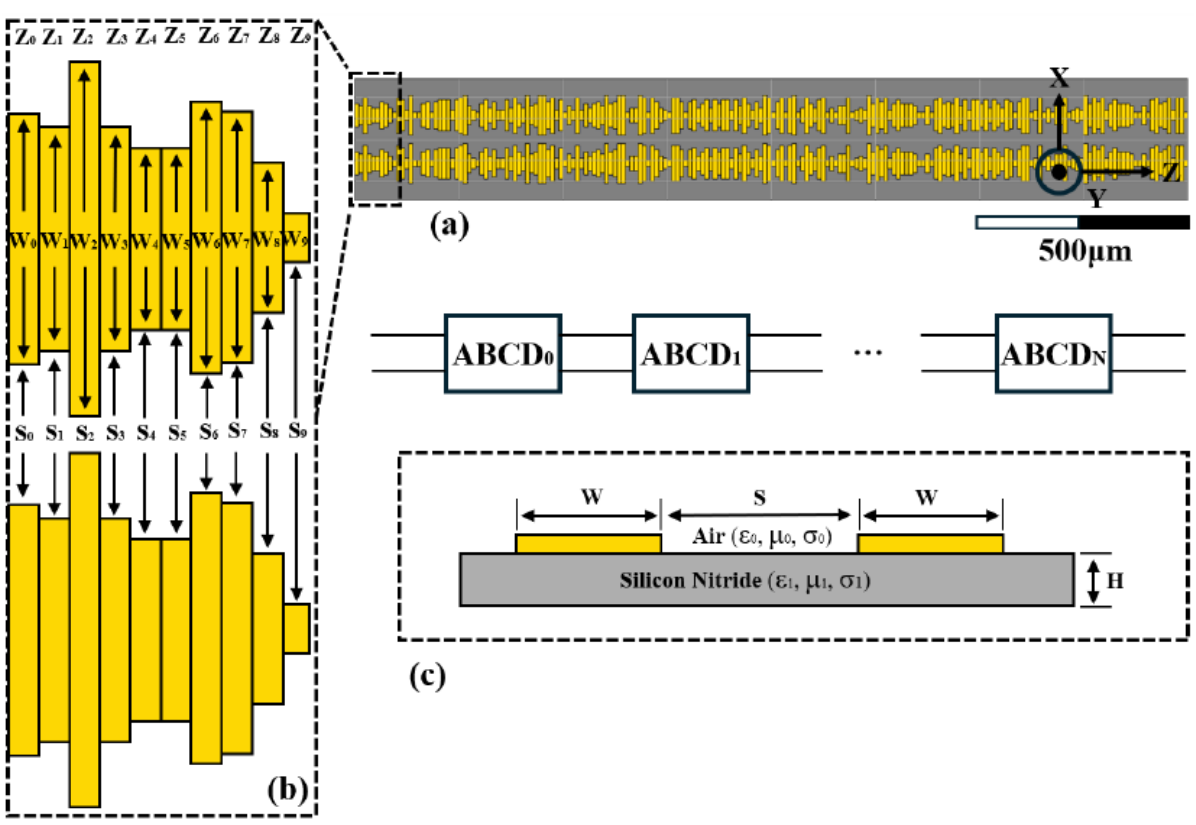

Figure 8 Illustration of the design framework and geometric parameters of the planar terahertz filter. (a) Example of a GA-optimized CPS-based THz filter with overall dimensions of 300 μm × 2000 μm, divided into 200 discrete segments along the propagation axis. (b) Enlarged section of the structure showing the key design variables: characteristic impedance (Z), conductor width (W), and spacing between strips (S). (c) Cross-sectional view of the device, where gold conductors are patterned on a silicon-nitride (Si_3N_4) membrane substrate [32].

The primary objective of this chapter is to showcase how the proposed GA–ABCD hybrid framework enables the discovery of compact and non-intuitive terahertz filter geometries that would be difficult to design through conventional methods. In addition, this chapter aims to validate the analytical model developed for the optimization process by comparing its predictions

with detailed full-wave simulations conducted in ANSYS HFSS. Finally, the chapter provides a comprehensive analysis of the filter's performance, focusing on its frequency response, field confinement characteristics, and the convergence behavior of the optimization algorithm.

3.2. Genetic-Algorithm Implementation

3.2.1. Representation and Initialization

The GA mimics biological evolution through iterative processes of selection, crossover, and mutation applied to a population of candidate filter geometries. Each candidate—encoded as a binary matrix describing metallic and dielectric pixels—is evaluated by computing its S-parameters using the ABCD-matrix method. Fitness is assigned according to how well its response matches the target magnitude and phase.

Each candidate design is encoded as a binary matrix of size M×N, where "1" represents gold and "0" represents air. In this work, the filter length of 2000 μm is divided into 200 columns (10 μm each), and the height into 30 rows (10 μm each), giving adequate spatial resolution while remaining computationally feasible.

The overall process, summarized in Figure 8, begins with the initialization of a random population of candidate filter geometries encoded as binary matrices. Each individual is evaluated using the ABCD matrix method to compute its S-parameters, including both magnitude and phase responses. These responses are then compared with the target specifications to assign a fitness value.

Based on this fitness, a selection process identifies the most promising candidates, which are then used to generate a new population through crossover and mutation operations. This iterative process continues across generations until a convergence criterion is met. The intermediate plots in Figure 9 illustrate how candidate designs evolve over successive generations, with progressively improved agreement between calculated and ideal responses. The final optimized design exhibits a magnitude response that closely matches the desired filter characteristics, along with a stable phase response.

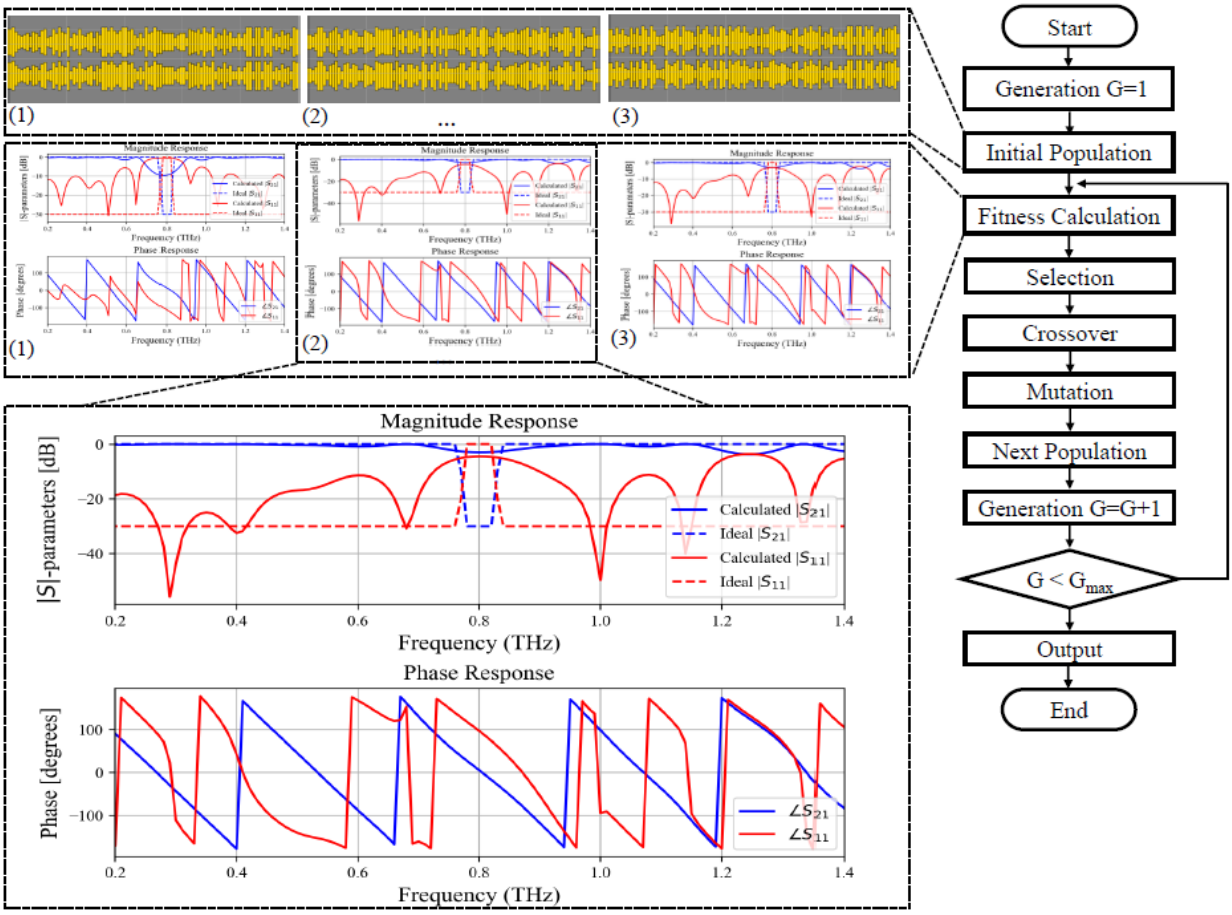

Figure 9 Flowchart of the GA optimization process. The diagram illustrates the workflow of the genetic algorithm, starting from the generation of an initial random population of THz filter designs and their corresponding S-parameter evaluations in both magnitude and phase. The algorithm iteratively refines the population through successive generations until one of two termination conditions is reached—either the maximum number of generations (G_{max}) is completed, or the error function falls below the defined convergence threshold [32].

3.2.2. Fitness Function

The fitness value quantifies how closely the simulated response matches the target S-parameters and is expressed as the negative of the weighted RMSE between modeled and target responses:

$$L = \omega_1 RMSE(|S_{21}|) + \omega_2 RMSE(|S_{11}|) + \omega_3 RMSE([\angle S_{21}]) + \omega_4 RMSE([\angle S_{11}]) \quad (3.1)$$

with ω_1=ω_2=0.4 and ω_3=ω_4 =0.1 in early generations, shifting slightly toward phase weighting in later iterations to improve dispersion characteristics. The GA seeks to maximize fitness F=−L.

$$F = \sum_{i=1}^{N} \left[\omega_1 \left| S_{21}(f_i) - S_{21}^{target}(f_i) \right|^2 + \omega_2 \left| S_{11}(f_i) - S_{11}^{target}(f_i) \right|^2 \right], \quad (3.2)$$

where N is the number of frequency points, and ω_1 and ω_2 are weighting coefficients emphasizing transmission and reflection, respectively.

Lower fitness values correspond to better-performing designs. Early generations focus primarily on magnitude matching, while later stages include phase and group-delay accuracy.

To accelerate computation, the fitness function is evaluated using the ABCD-matrix model, which analytically estimates the transmission and reflection characteristics of each geometry without running full-wave simulations. This surrogate model makes it possible to evaluate hundreds of designs per minute, enabling efficient optimization.

3.2.3. Population and Selection

A population of 200 individuals was adopted to balance search breadth and computational load. The elite fraction—top 15 % of the population—was retained unchanged between generations to preserve the best designs. Selection used a rank-based tournament with size T=4 and pressure s=0.8:

$$P(i) = \frac{(1-s)s^{r_i-1}}{1-s^T} \quad (3.2)$$

where r_i is the rank of individual i (1 = best). This probabilistic method encourages diversity while favoring high-fitness solutions [33], [34].

3.2.4. Crossover and Mutation

A two-point crossover scheme exchanges design segments between two parent chromosomes:

$$O_1 = [P_1(:,1:c_1), P_2(:,c_1:c_2), P_1(:,c_2:C)\,] \quad (3.3)$$

$$O_2 = [P_2(:,1:c_1), P_1(:,c_1:c_2), P_1(:,c_2:C)\,] \quad (3.4)$$

where c_1 and c_2 are randomly chosen crossover points along the 200-column design grid.

In this implementation, mutation is performed by randomly flipping individual bits (changing “1” to “0” or vice versa) within the binary matrix. This operation changes the local metallic or dielectric state of small pixel regions, introducing new geometric variations.

A mutation rate of 10% was used, meaning that approximately one-tenth of the pixels in the population are randomly altered in each generation. The rate is carefully chosen to maintain diversity without introducing excessive randomness that could destabilize convergence.

To ensure that progress is not lost between generations, the GA employs an elitism strategy, in which a small percentage of the best-performing designs (about 15%) are directly copied into the next generation without modification. Figure 10 shows the operation enables the exchange of inherited characteristics between parents, promoting diversity and improving the optimization of the filter's electromagnetic performance.

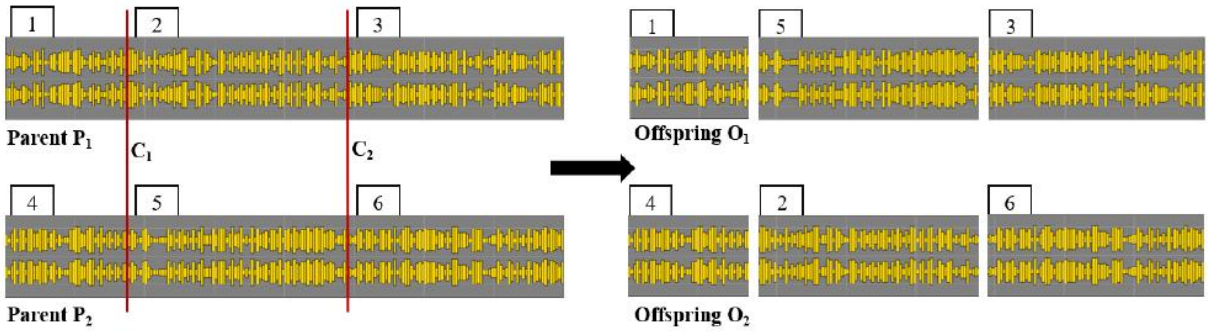

Figure 10 Illustration of the two-point crossover mechanism used in the GA-based inverse design of THz filters. The diagram demonstrates how structural features from two parent geometries are recombined through the crossover process to create new offspring designs [32].

Elitism preserves the most promising candidates and provides a stable reference for evaluating subsequent generations. This mechanism accelerates convergence and ensures that the population never regresses in performance.

3.3. ABCD-Matrix Evaluation

A key innovation in this work is the integration of the ABCD matrix model as a surrogate analysis tool within the optimization loop. This model provides an analytical method for evaluating each candidate design's transmission and reflection characteristics without resorting to time-consuming full-wave electromagnetic simulations.

Each column of the discretized filter is modeled as a uniform transmission-line segment with characteristic impedance Z_i and propagation constant β_i. The ABCD matrix of a single segment of length Λ is

$$\begin{bmatrix} A_i & B_i \\ C_i & D_i \end{bmatrix} = \begin{bmatrix} \cos(\beta_i \Lambda) & jZ_i \sin(\beta_i \Lambda) \\ j\frac{1}{Z_i}\sin(\beta_i \Lambda) & \cos(\beta_i \Lambda) \end{bmatrix} \tag{3.4}$$

and the total transfer matrix for N cascaded sections is the product of all individual matrices:

$$\begin{bmatrix} A & B \\ C & D \end{bmatrix}_{total} = \prod_{i=1}^{N} \begin{bmatrix} A_i & B_i \\ C_i & D_i \end{bmatrix} \quad (3.5)$$

Each section's characteristic impedance is estimated analytically from its conductor width W_i and gap S_i using the quasi-static formula for coplanar striplines [31]:

$$Z_{CPS_i} = \frac{120\pi}{\sqrt{\varepsilon_{re}}} \frac{K(k_i')}{K(k_i)}, \quad k_i = \frac{S_i}{S_i + 2W_i} \quad (3.4)$$

Here K(k) is the complete elliptic integral of the first kind and ε_{re} the effective relative permittivity of the Si_3N_4 substrate.

Finally, the scattering parameters are computed from the composite ABCD matrix obtain from eq. 2.4. where $Z_0=Z_{CPS}$ is the reference impedance. This analytical approach offers a computational speed-up of >1000× compared with full-wave finite-element simulations, allowing evaluation of all 200 individuals per generation. Thousands of design candidates can thus be evaluated per generation, allowing the GA to efficiently explore large and complex design spaces. The top-performing geometries identified by the ABCD-based model are then verified using HFSS to ensure full electromagnetic consistency [15].

3.4. General Simulation Configuration

This platform provides a Python-based graphical interface that enables users to define filter specifications, control GA parameters, and automatically export the final design to HFSS for validation [35].

In the HFSS configuration (Figure 11), the setup frequency was set to 1.0 THz, with a discrete sweep from 0.2 THz to 1.2 THz using a step size of 0.01 THz. The simulation included 10 adaptive passes and a maximum ΔS of 0.1, ensuring field convergence and accurate extraction of scattering parameters (S_{11} and S_{21}). This configuration provided a stable trade-off between speed and accuracy for THz simulations.

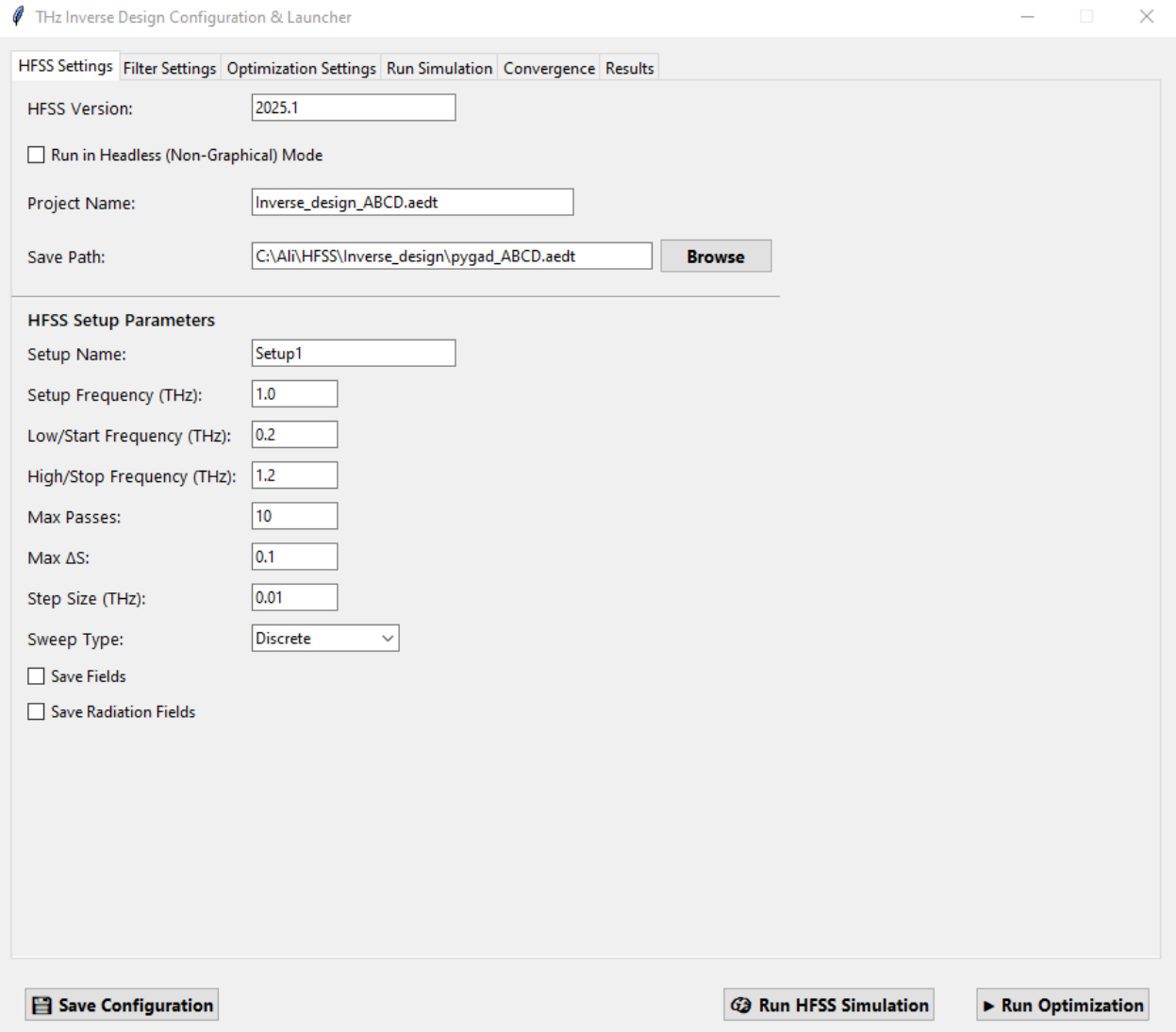

Figure 11 HFSS Settings tab showing frequency sweep setup (0.2–1.2 THz) [35].

The design target was a planar low-pass THz filter, as shown in Figure 12 The cutoff frequency was 0.6 THz with a 3 dB bandwidth of 0.14 THz and a stopband depth of −40 dB. The transition bandwidth was set to 0.03 THz to ensure steep roll-off behavior. The software generated an ideal magnitude and phase response, serving as the optimization target.

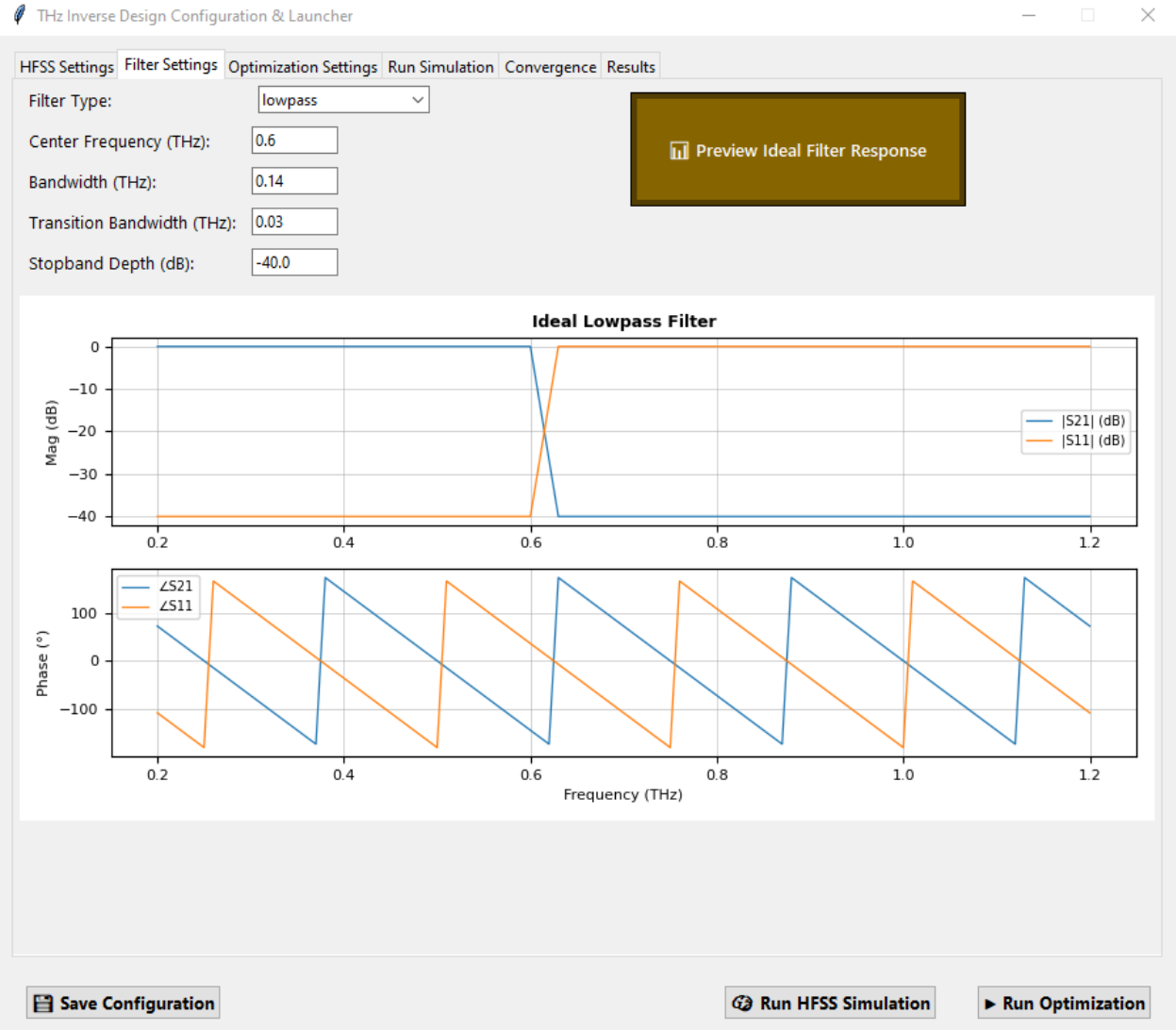

Figure 12 Filter Settings tab showing target low-pass filter response at 0.6 THz cutoff.

For optimization (Figure 13), the Genetic Algorithm was selected with the following parameters: 120 generations, population size of 200, 20 mating parents, 10 elite individuals, and a mutation probability of 0.1. Each optimization run took approximately 40 minutes on an Intel i7-10700 CPU at 3.8 GHz. The fitness function minimized the root-mean-square error (RMSE) between the analytical ABCD response and the target ideal filter. Convergence was achieved near generation 110 when RMSE improvements dropped below 0.5% per 10 generations.

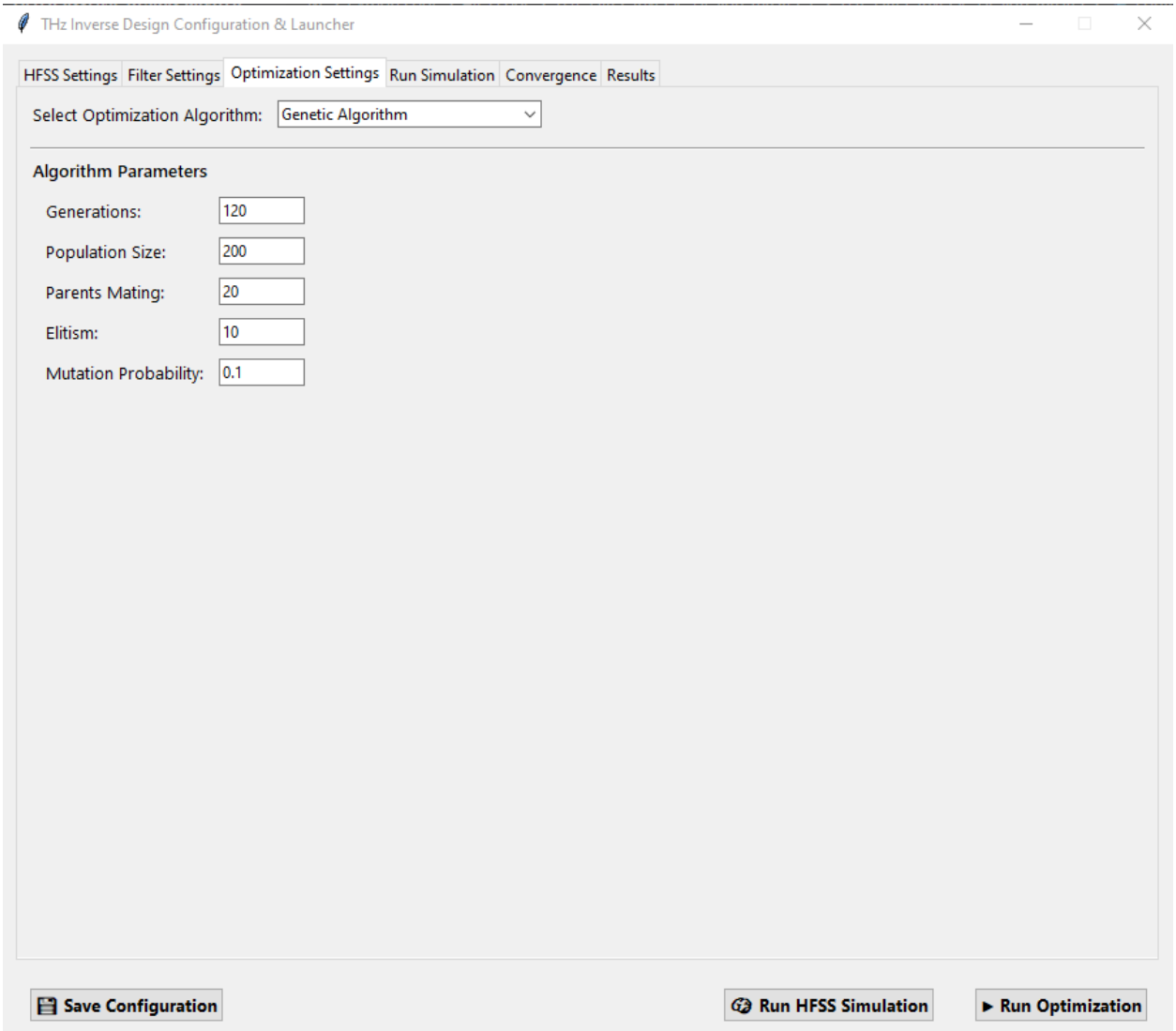

Figure 13 Optimization Settings tab showing GA configuration parameters.

The final optimized low-pass filter exhibited a 3 dB cutoff frequency of approximately 0.61 THz, an in-band insertion loss below 1.5 dB, and stopband rejection exceeding −40 dB. The nearly linear phase response across the passband confirmed low-dispersion characteristics, validating the GA–ABCD framework as an effective tool for compact THz filter design.

3.5. Full-Wave Validation Using HFSS

The final geometry was exported from the Python launcher to ANSYS HFSS 2025.1 for full-wave electromagnetic simulation. The HFSS setup included a discrete frequency sweep from 0.2 THz to 1.2 THz with a 0.01 THz step size and 10 adaptive passes. The calculated S-parameters were compared to those from the ABCD analytical model to verify accuracy.

As shown in Figure 14, both HFSS and ABCD results displayed consistent low-pass characteristics with a 3 dB cutoff near 0.6 THz. Below the cutoff, $|S_{21}|$ remained close to 0 dB, while $|S_{11}|$ stayed below −15 dB, confirming proper impedance matching. Strong attenuation (>40 dB) was achieved above 0.8 THz, validating the filter's ability to suppress high-frequency components.

Small deviations between HFSS and ABCD results, particularly in phase response at higher frequencies, were attributed to fringing effects and material dispersion not captured by the analytical model. Overall, the close agreement demonstrated the reliability of the ABCD-based optimization before high-fidelity validation.

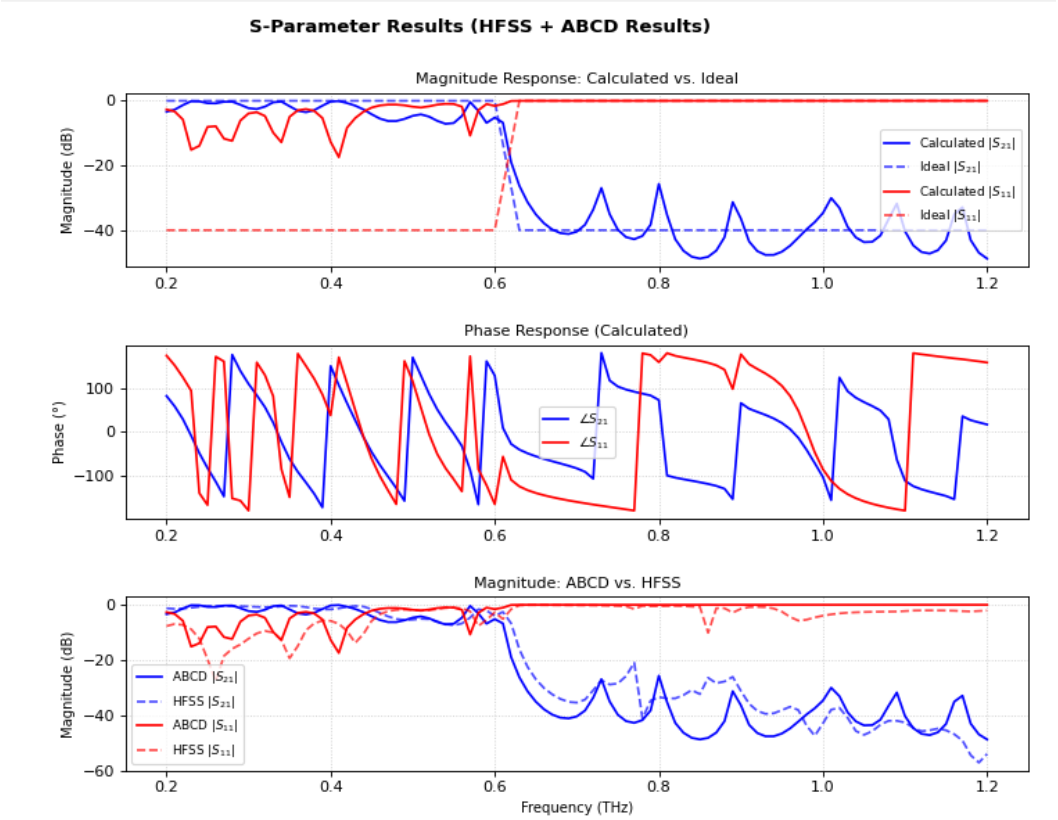

Figure 14 Comparison of HFSS and ABCD S-parameter results for the optimized low-pass filter.

3.6. Performance Analysis

The performance of the optimized low-pass filter was evaluated based on frequency response, phase behavior, and convergence performance. The filter showed minimal insertion loss (<1.5 dB)

within the passband (0.2–0.6 THz) and over −40 dB rejection in the stopband. The transition between passband and stopband occurred sharply between 0.6 and 0.7 THz.

The phase response remained nearly linear across the passband, suggesting low group-delay variation and minimal dispersion—essential features for THz communication systems.

The optimization convergence trend is presented in Figure 15. The fitness value improved rapidly within the first 40 generations and gradually stabilized near generation 110. The RMSE decreased below 0.5%, indicating a steady and efficient convergence. This behavior confirmed the GA's robustness in navigating the binary design space.

This hybrid GA–ABCD–HFSS framework significantly reduced computation time compared to traditional full-wave-only methods while maintaining high accuracy. The system can also support other optimization strategies such as Particle Swarm Optimization (PSO) and the Adjoint Method for future extensions.

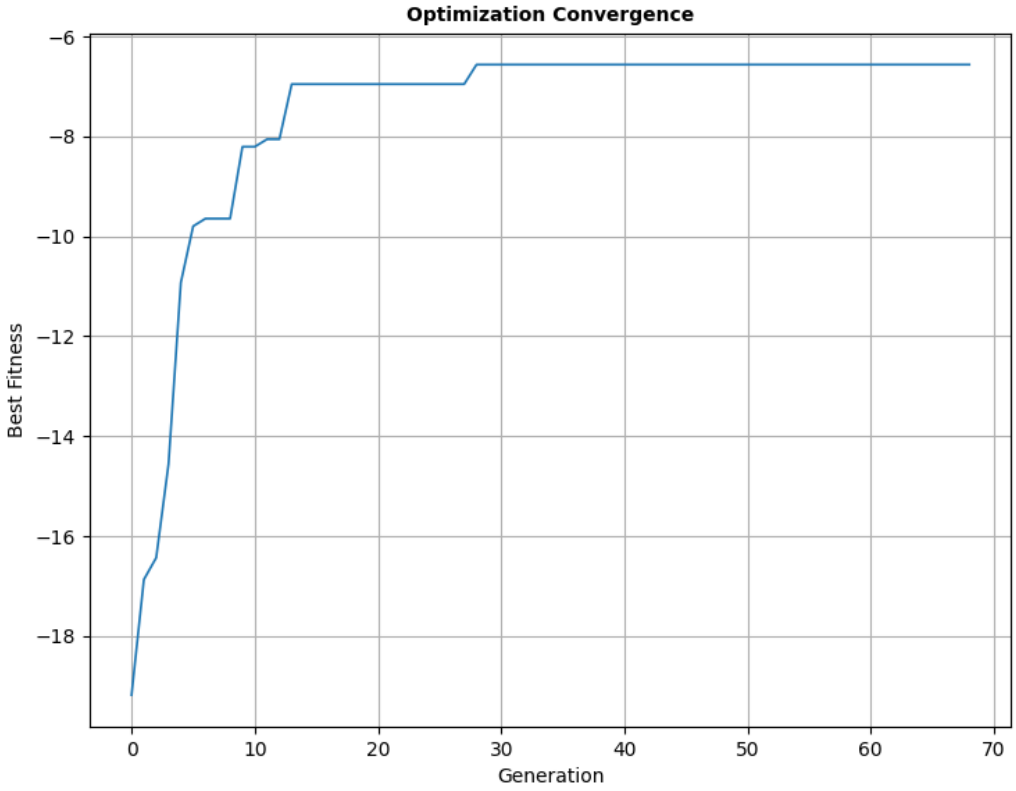

Figure 15 Optimization convergence curve for the GA-based low-pass filter design.

4. Multi-Frequency Validation of the GA-ABCD Framework

4.1. Objective of Validation

The computational framework used in this project was originally developed by Ali Dehghanian [35] [15] as part of his doctoral research on genetic-algorithm-based inverse design of guided-wave planar terahertz filters. His work established the main optimization code, including the genetic algorithm structure, the binary geometry representation, the ABCD-matrix-based evaluation method, and the workflow for generating filter geometries for electromagnetic validation.

The contribution of this project was not the original development of the optimization code itself, but rather the validation, extension, and evaluation of the existing framework across multiple operating frequencies and filter responses. In this work, the previously developed code was applied to a wider range of target frequencies, from 0.25 THz to 2.0 THz, for both low-pass and band-stop filter configurations. For each case, the optimization results were examined using the ABCD matrix model and then compared with full-wave HFSS simulations to evaluate whether the framework remained accurate and stable beyond the original design case.

A major part of this contribution involved systematically changing and documenting simulation parameters such as the number of rows in the discretized geometry, the effective permittivity used in the analytical model, the HFSS setup frequency, the frequency sweep range, and the convergence threshold. These adjustments were introduced in a controlled way to maintain stable optimization and reliable full-wave validation as the target frequency increased. The resulting comparisons provided insight into the strengths and limitations of the GA–ABCD approach, especially at higher frequencies where parasitic effects, dispersion, fringing fields, and geometric sensitivity become more significant.

Therefore, this project extends Ali Dehghanian's original framework by demonstrating its applicability over a broader frequency range and by identifying how its performance changes under different design conditions. The work contributes a multi-frequency validation study that helps clarify where the analytical ABCD model remains reliable, where HFSS validation becomes essential, and how the framework may be further improved for practical THz filter design.

4.2. Simulation Configuration and Parameter Adjustments

The baseline simulation parameters used in Chapter 3 were selected to provide a balance between computational efficiency and spatial resolution. These parameters were sufficient for low-frequency designs and served as the reference configuration for this study. Furthermore, the chosen parameter set is sufficient for demonstrating the validity of the proposed framework as a proof-of-concept, rather than representing a fully optimized or application-specific design configuration.

The primary configuration included a discretized grid of 18 rows and 200 columns, with a coplanar strip width of 10 μm, rectangular unit width of 5 μm, and a cell length of 10 μm. The effective permittivity was set to 1.45, consistent with the thin-membrane CPS approximation.

However, during the extension of the framework to higher-frequency designs, it became necessary to adjust certain parameters within the code to maintain numerical stability and ensure accurate representation of the electromagnetic behavior.

At higher frequencies, the wavelength becomes smaller, and the electromagnetic response becomes more sensitive to geometric resolution. As a result, modifications were introduced to the discretization and model parameters to better capture the finer structural variations required for accurate filter synthesis.

These changes were applied in a controlled manner, without altering the core optimization framework, fitness function, or genetic algorithm workflow.

Frequency (THz)	Generation	Rows	ε_{eff}	Fitness at Convergence (dβ)	Setup Frequency (THz)	Low Frequency (THz)	High Frequency (THz)	Max Δs	Convergence Trend	Observation
0.25	150	18	1.42	-10.200	1.0	0.1	1.2	0.1	Smooth, gradual	Slower convergence, stable response
0.5	150 stops at 129	18	1.45	-5.498	1.0	0.2	1.2	0.1	Smooth	Good agreement with ideal response
0.75	150 stops at 85	18	1.45	-6.543	1.0	0.2	1.3	0.1	Fast early convergence	Stable, consistent behavior
1.00	120 stops at 107	14	1.45	-5.464	1.0	0.5	1.5	0.1	Faster convergence	Reduced grid improved stability
1.25	150	14	1.45	-4.932	1.0	0.7	1.75	0.1	Stable	Slight tuning needed

1.5	120	14	1.45	-6.350	1.6	1.0	2.0	0.02	Stable	Sharper transition region
1.75	120	12	1.40	-5.434	1.9	1.3	2.2	0.02	Stable but sensitive	Further reduction required
2.00	120	12	1.40	-6.347	2.0	1.6	2.5	0.02	Rapid convergence	Highest frequency, strongest adjustment

Table 1 Different frequency of low-pass filter

Table 1 summarizes the optimization and validation settings used for the low-pass filter cases across the tested frequency range from 0.25 THz to 2.00 THz. Its purpose is to show how the same GA–ABCD–HFSS workflow was applied to multiple low-pass targets while only a limited number of parameters were adjusted as the target frequency increased. This table is important because it demonstrates that the framework was not tuned for only one example; instead, it was tested across a wider range of operating conditions to evaluate both its stability and its practical limits.

The first column, Frequency (THz), gives the target operating frequency used for each low-pass design case. In the context of Table 1, this frequency corresponds to the intended cutoff region of the filter. By presenting multiple target frequencies, the table makes it possible to observe how the inverse-design framework behaves as the operating point shifts from the lower THz range to higher-frequency cases, where the electromagnetic response becomes more sensitive to geometry and validation settings.

The Generation column indicates how many GA generations were used or reached during each optimization run. In several cases, the optimization stopped before the full generation limit, which suggests that the fitness had stabilized early and that further iterations were not producing meaningful improvement. This is useful because it shows that convergence behavior was not identical across all frequencies. Lower-frequency cases tended to converge smoothly, while some mid-frequency cases reached stable solutions earlier than the maximum allowed number of generations.

The Rows column gives the number of rows used in the discretized geometry grid. This parameter controls the vertical resolution of the candidate filter structure. At lower frequencies, the design used 18 rows, which gave the optimizer sufficient geometric flexibility. As the target frequency increased, the number of rows was reduced first to 14 and then to 12. This reduction reflects a

practical modeling choice: at higher frequencies, the response becomes more sensitive to small structural variations, and reducing the number of rows helps keep the search space more stable and computationally manageable. In this way, the table shows that the framework was not arbitrarily changed but rather adjusted in a controlled way to maintain robustness.

The ε_{eff} column lists the effective permittivity used in the ABCD model. This parameter is important because it directly affects the predicted propagation constant and phase behavior of the coplanar stripline structure. For most of the low-pass cases, the effective permittivity remained near 1.45, which is consistent with a membrane-supported CPS structure where a large portion of the field propagates in air. At the highest frequencies, the value was slightly reduced to 1.40, indicating a small retuning of the analytical model to maintain physically reasonable agreement as the operating band shifted upward.

The Fitness at Convergence column reports the best fitness value obtained for each case. Since the fitness is defined as the negative of the weighted error, values closer to zero correspond to a better match between the calculated response and the ideal target. The values reported in Table 1 remain within a relatively narrow range, which suggests that the framework was able to maintain a comparable level of optimization quality across the tested low-pass frequencies. At the same time, differences among these values indicate that some target frequencies were naturally easier to match than others.

The Setup Frequency (THz) column gives the adaptive setup frequency used in HFSS. This parameter determines where the full-wave solver focuses its mesh refinement. At lower and mid frequencies, the setup frequency remained at 1.0 THz, which provided a reasonable balance between simulation accuracy and computational efficiency. For the higher-frequency cases, the setup frequency was increased to 1.6 THz, 1.9 THz, and 2.0 THz, respectively. This is a physically sensible adjustment, since higher-frequency simulations require the mesh to remain accurate in a more demanding part of the spectrum.

The Low Frequency (THz) and High Frequency (THz) columns define the HFSS sweep range used for validation. These ranges were adjusted so that the simulation window always covered the important passband, transition region, and stopband associated with each target cutoff. This is significant because a fixed sweep range would not be equally appropriate for all frequency cases.

By shifting the sweep window upward as the target frequency increased, the validation remained focused on the most relevant portion of the response.

The Max ΔS column gives the HFSS convergence threshold between adaptive passes. For frequencies up to 1.25 THz, the threshold remained at 0.1, which was adequate for the lower-frequency cases. For 1.5 THz and above, the threshold was tightened to 0.02. This change indicates that the higher-frequency cases required stricter full-wave convergence in order to obtain more reliable validation results. This is consistent with the expectation that, as frequency increases, the solution becomes more sensitive to mesh quality and to higher-order electromagnetic effects.

The Convergence Trend column gives a qualitative description of how the optimization progressed. Terms such as smooth, fast early convergence, stable, and stable but sensitive help clarify the optimization behavior beyond the final fitness value alone. For example, the lower-frequency cases show smoother or more gradual convergence, while some higher-frequency cases are described as stable but more sensitive. This suggests that although the framework remained usable at high frequency, the optimization became less forgiving and required more careful parameter control.

Finally, the Observation column provides a short practical interpretation for each case. These remarks help connect the numerical settings with the actual behavior of the optimization. For instance, the table notes that the 0.5 THz case showed good agreement with the ideal response, while the 1.75 THz and 2.00 THz cases required stronger adjustment and exhibited higher sensitivity. This makes the overall trend easier to understand: the framework performs strongly at lower frequencies and remains functional at higher frequencies, but the higher-frequency cases demand tighter validation settings and more careful tuning.

Frequency (THz)	Generation	Rows	ε_{eff}	Fitness at Convergence (dβ)	Setup Frequency (THz)	Low Frequency (THz)	High Frequency (THz)	Max Δs	Convergence Trend	Observation
0.25	150	18	1.42	-4.660	1.0	0.1	1.0	0.1	Gradual, slower	Wide stopband, stable but slower convergence
0.5	150	18	1.42	-4.802	1.0	0.1	1.0	0.1	Smooth	Good agreement, moderate oscillations
0.75	150 stops at 103	18	1.42	-4.336	1.0	0.2	1.2	0.1	Fast early convergence	Stable response,

										improved matching
1.00	150	14	1.38	-4.644	1.2	0.5	1.5	0.02	Faster convergence	Reduced rows improved stability
1.25	150	14	1.43	-4.660	1.44	0.8	1.8	0.02	Stable	Slight parameter tuning required
1.5	120	14	1.45	-3.935	1.8	0.8	2.25	0.02	Rapid convergence	Increased sensitivity, sharper notch
1.75	120	14	1.45	-4.723	1.8	1.2	2.3	0.02	Stable plateau	Good notch formation but fluctuations present
2.00	120	12	1.38	-4.844	2.0	1.5	2.5	0.02	Smooth plateau	Highest frequency, strongest parameter adjustment

Table 2 Different frequency of band-stop filter

Table 2 presents the optimization and validation settings for the band-stop filter cases. In general, the overall workflow is the same as the low-pass study shown in Table 1. The same GA–ABCD–HFSS framework is used, the same inverse-design logic is followed, and the same general sequence is preserved: first, the optimizer searches for a geometry using the fast ABCD-based evaluation, and then the final design is validated using HFSS. However, the main difference between the band-stop and low-pass cases is the physical mechanism of the filter response. At lower center frequencies (0.25–0.75 THz), the original configuration with 18 rows and an effective permittivity of approximately 1.42 provides stable responses. However, convergence is slower at 0.25 THz due to the wider stopband, while higher frequencies within this range show faster convergence and improved matching.

A noticeable feature of Table 2 is that the value of ε_{eff}varies more across the band-stop cases than it does in the low-pass study. This is mainly because the band-stop response is governed by a localized resonant notch, which is much more sensitive to phase delay and effective electrical length than a low-pass cutoff. In the ABCD model, ε_{eff}influences the propagation constant and therefore directly affects the predicted notch location, rejection depth, and phase response. As the target frequency increases, the field distribution and the balance between air-guided and substrate-influenced propagation can change, so a single fixed effective permittivity is not always sufficient

to maintain good agreement between the analytical model and the expected physical response. For this reason, $\varepsilon_{eff}$was adjusted in a controlled way across the band-stop cases to keep the surrogate model physically meaningful and to preserve accurate placement of the resonant stopband. This variation does not indicate inconsistency in the workflow; rather, it reflects the greater sensitivity of the band-stop filter to frequency-dependent propagation behavior.

At higher frequencies (1.5–2.0 THz), the system becomes more sensitive, and further parameter adjustments are required. Although the number of rows remains at 14 up to 1.75 THz, the convergence becomes faster but exhibits increased sensitivity, particularly in the notch region. At 2.0 THz, the number of rows is reduced further to 12 to ensure stable convergence and maintain a well-defined stopband.

The fitness values remain within a relatively narrow range across all cases, indicating that the optimization process is robust. While higher frequencies introduce fluctuations and increased sensitivity, the method is still able to produce a clear band-stop response with acceptable accuracy.

4.3. Frequency Response Analysis

4.3.1. Low-Pass Filter Response

The performance of the low-pass filter is evaluated across multiple cutoff frequencies and grouped into three ranges to highlight general trends.

4.3.1.1. Low Frequencies

At lower cutoff frequencies, the low-pass filter as shown in Figure 16(a–c) exhibits a smooth transition between passband and stopband. The transmission coefficient |S21| remains close to 0 dB in the passband and gradually rolls off beyond the cutoff frequency.

The stopband attenuation is moderate, and the transition region is relatively wide. This indicates limited selectivity at lower frequencies. The reflection coefficient |S11| shows noticeable variation, suggesting that impedance matching is not ideal across the entire passband.

The ABCD-based analytical results align closely with HFSS simulations in this range. The overall shape of the response is well captured, and deviations are minimal, especially near the cutoff region.

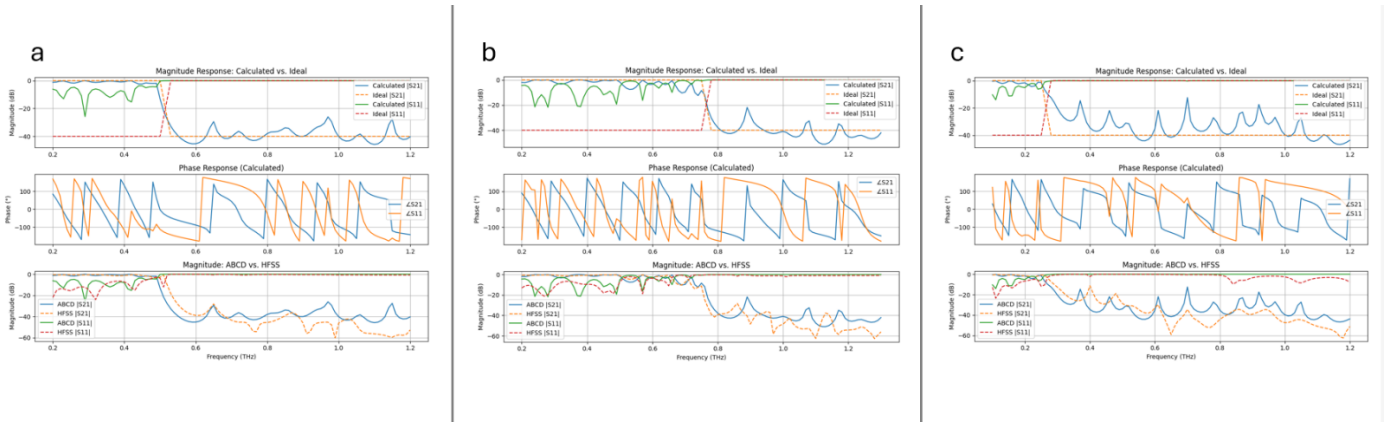

Figure 16 lower cutoff frequencies a) 0.25 b) 0.5 c) 0.75 THz

4.3.1.2. Mid Frequencies

As the cutoff frequency increases, the transition between passband and stopband becomes sharper, as shown in Figure 17(a-c). The roll-off of |S21| improves, indicating better selectivity compared to the low-frequency case.

The passband remains relatively flat, with reduced variation in |S11| across the passband, as observed in Figure 17(a–c), indicating improved impedance matching relative to lower frequencies. However, small ripples begin to appear in both the magnitude and phase responses.

The agreement between the analytical model and HFSS remains strong near the cutoff frequency, but slight discrepancies begin to appear in the stopband region. These differences are mainly observed as variations in attenuation depth and ripple behavior.

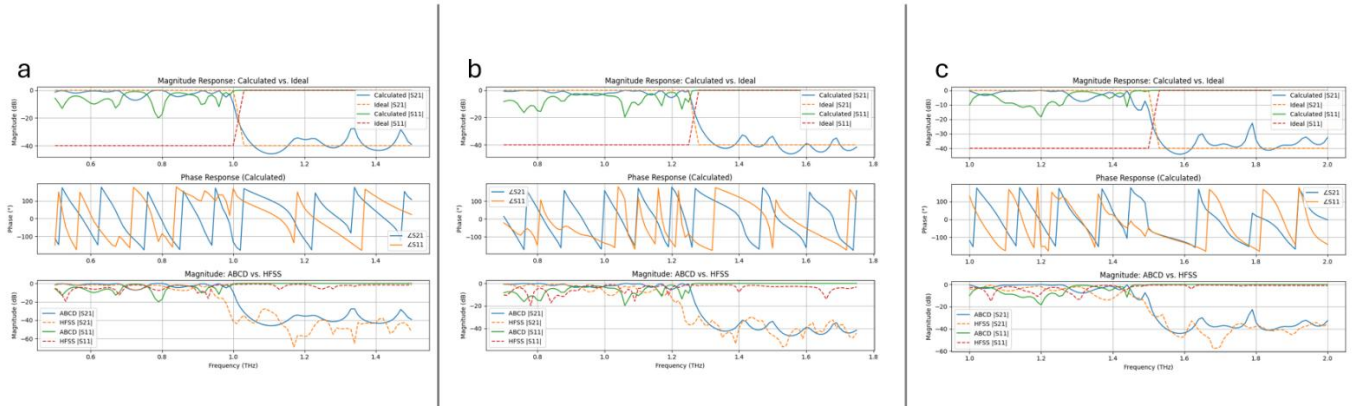

Figure 17 Mid cut off frequencies a) 1.0 b) 1.25 c) 1.5 THz

4.3.1.3. High Frequencies

At higher cutoff frequencies, the filter maintains its overall low-pass behavior, but the response becomes more irregular, as shown in Figure 18(a–b). The stopband attenuation increases, but the ripple becomes more pronounced, particularly in the HFSS results.

This degradation in performance at higher frequencies can be attributed to several factors. First, as the operating frequency increases, the electrical size of the structure becomes larger relative to the wavelength, making the system more sensitive to geometric discretization and grid resolution. Second, higher frequencies amplify parasitic effects, including fringing fields, conductor losses, and substrate-related dispersion, which are not fully captured by the simplified analytical model.

While the analytical model continues to predict the cutoff frequency accurately, its ability to capture fine details diminishes. The HFSS results therefore show stronger deviations, reflecting the increased electromagnetic complexity at higher frequencies.

Overall, the low-pass filter maintains consistent qualitative behavior across all frequencies; however, higher-frequency designs exhibit increased ripple and deviation due to the combined effects of discretization limits, parasitic phenomena, and model simplifications.

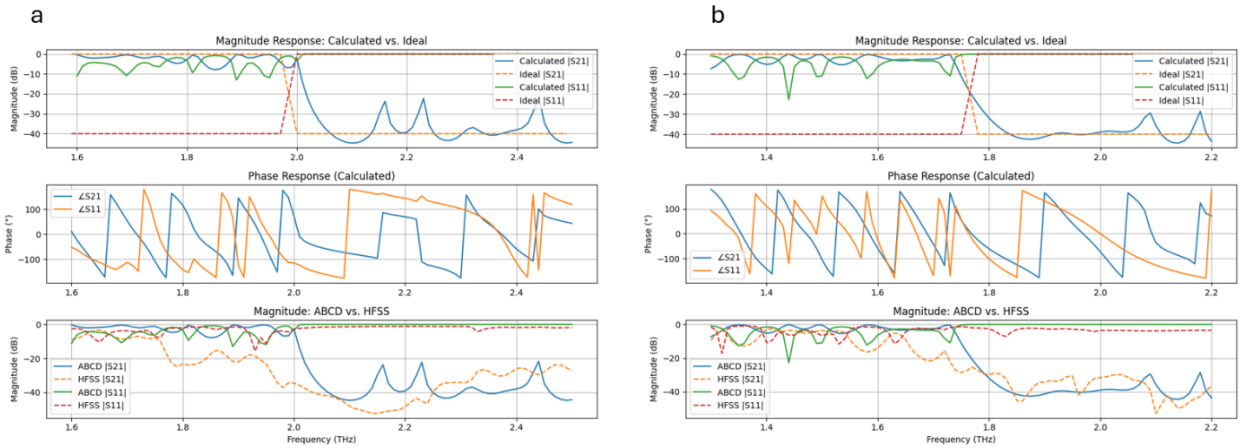

Figure 18 High cut off frequencies a) 1.75 b) 2.0 THz

4.3.2. Band-Stop Filter Response

The band-stop filter is analyzed using the same frequency grouping to allow direct comparison of behavior across the spectrum.

4.3.2.1. Low Frequencies

At lower center frequencies, the band-stop filter exhibits a relatively broad stopband. The attenuation in |S21| is present but not sharply defined, resulting in a wide and shallow notch.

The reflection coefficient |S11| shows significant variation across the frequency range, indicating imperfect impedance matching. Compared to the low-pass filter, the response is more sensitive to frequency changes even at this stage.

The analytical and HFSS results show good agreement near the center frequency, but HFSS introduces additional ripple outside the stopband that is not captured by the analytical model.

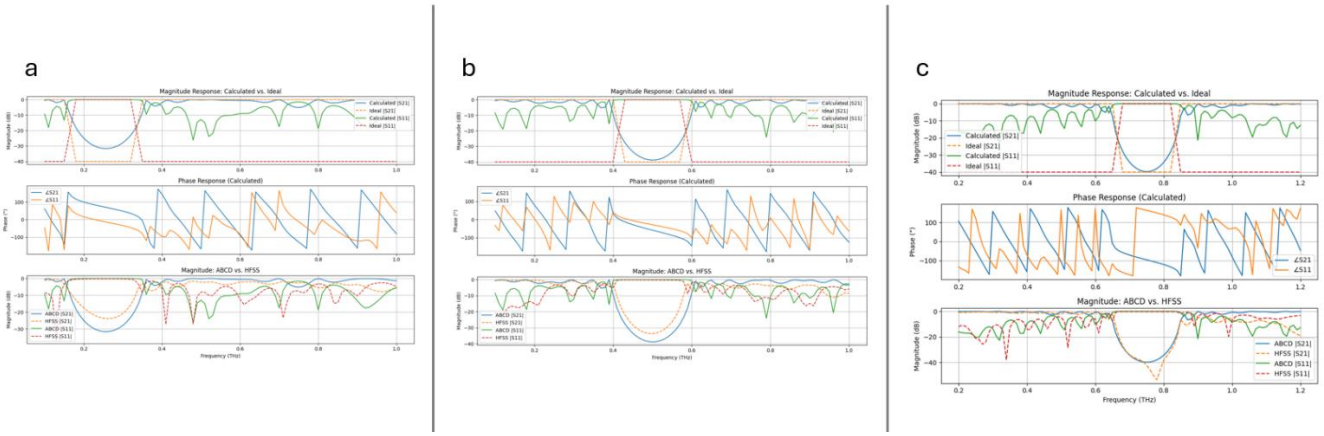

Figure 19 lower cutoff frequencies a) 0.25 b) 0.5 c) 0.75 THz

4.3.2.2. Mid Frequencies

At mid-range center frequencies, shown in Figure 20(a-c), the band-stop behavior becomes more pronounced. The notch in |S21| becomes deeper and more localized, indicating improved selectivity.

The transition into and out of the stopband is sharper compared to the low-frequency case. The phase response also shows more abrupt changes, consistent with the sharper magnitude transitions.

However, discrepancies between ABCD and HFSS results become more noticeable. The HFSS response exhibits increased ripple and variations in the stopband floor, highlighting the influence of effects not included in the analytical model.

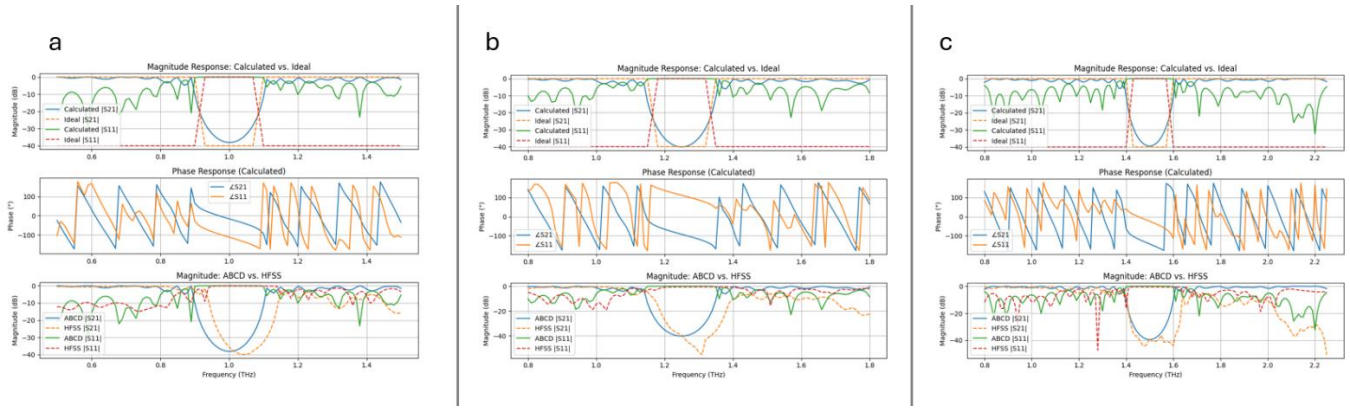

Figure 20 Mid cut off frequencies a) 1.0 b) 1.25 c) 1.5 THz

4.3.2.3. High Frequencies

At higher center frequencies, the band-stop filter maintains its notch behavior, but the differences between analytical and simulation results increase significantly.

The HFSS results show stronger ripple, deeper fluctuations, and higher losses within the stopband. While the analytical model continues to predict the center frequency accurately, it fails to capture the detailed behavior of the response.

These deviations are more pronounced than in the low-pass filter case, indicating that band-stop structures are more sensitive to high-frequency effects such as higher-order modes.

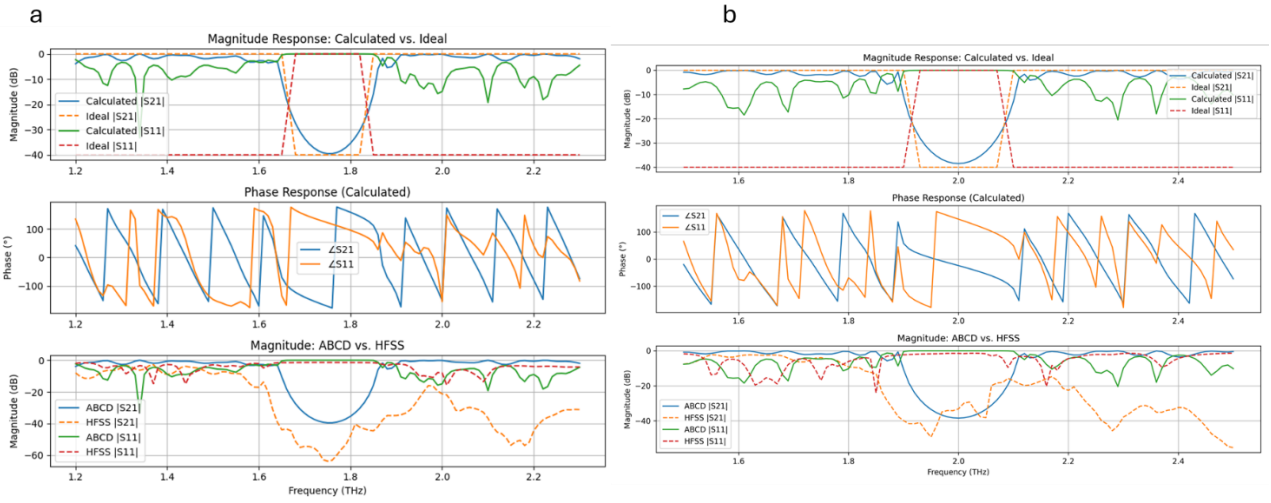

Figure 21 High cut off frequencies a) 1.75 b) 2.0 THz

4.4. Discussion: Analytical Model and HFSS Simulation

The comparison between the analytical ABCD matrix model and full-wave HFSS simulations confirms that the implemented code provides an accurate and computationally efficient representation of the electromagnetic behavior of the designed THz filters. The agreement observed across both low-pass and band-stop responses demonstrates that the analytical formulation successfully captures the dominant propagation and resonance mechanisms governing the structures.

The ABCD model is based on a quasi-static transmission-line approximation, where each unit cell is treated as a uniform segment characterized by its impedance and propagation constant, and the overall response is obtained through cascading these matrices. This formulation enables rapid evaluation of S-parameters using closed-form transformations, making it particularly suitable for optimization frameworks such as the genetic algorithm used in Ali Dehghanian's work. As a result, the model provides a strong approximation of the spectral response while maintaining computational efficiency that is several orders of magnitude faster than full-wave methods .

Across all frequency ranges, the most consistent agreement between the ABCD and HFSS results occurs at the key design frequencies, specifically the cutoff frequency for low-pass filters and the center (notch) frequency for band-stop filters. This is because these frequencies correspond to the dominant design constraints of the filter, where the optimization process explicitly enforces the desired transmission behavior. At these points, the response is primarily governed by overall phase accumulation and impedance transformation, which are well captured by the ABCD formulation.

In contrast, away from these key frequencies, the response becomes more sensitive to higher-order effects such as parasitic coupling, dispersion, and local field variations, which are not fully represented in the analytical model. As a result, both approaches predict nearly identical transmission characteristics at the design frequencies, while discrepancies increase outside these regions. This is consistent with the findings in Ali Dehghanian's work [15], where strong agreement between the ABCD predictions and HFSS simulations was reported near the primary operational frequencies.

However, deviations become more pronounced at higher frequencies. The HFSS results exhibit additional attenuation variations, ripple, and phase irregularities that are not present in the

analytical curves. These discrepancies arise from physical effects that are not included in the quasi-static ABCD formulation. In particular, radiation losses, edge diffraction, and imperfect field confinement become increasingly significant as frequency increases and the wavelength approaches the geometric dimensions of the structure. These effects were explicitly identified in Ali Dehghanian's work as the primary source of divergence between analytical and full-wave results beyond the designed frequency range.

The band-stop filters show a stronger sensitivity to these effects compared to the low-pass filters. This behavior is consistent with the results presented in Figure 19(a–c), where increased ripple and deviation are observed near the stopband frequencies. From a physical standpoint, band-stop behavior is governed by localized resonances within the structure, where energy is temporarily stored and strongly interacts with the geometry.

As demonstrated in Figure 19(a–c), these resonances correspond to strong field confinement at the stopband frequency, resulting in significant attenuation of transmitted power. Because resonance phenomena amplify the impact of small perturbations, additional effects such as parasitic coupling, fabrication non-idealities, and higher-order modes lead to visible deviations in the HFSS response.

In contrast, the low-pass filters, as shown previously in Figure 16 and Figure 17, rely on distributed impedance transitions rather than sharp resonances. This results in a smoother response that is inherently less sensitive to these secondary effects.

The phase response further highlights the limitations of the analytical model. While the ABCD formulation captures the general trend of phase progression, the HFSS results show more complex behavior, particularly near resonance regions and at higher frequencies. This difference is linked to dispersion and energy storage mechanisms that are only partially represented in the transmission-line approximation. Maintaining linear phase is critical in THz systems to avoid signal distortion, and the analytical model provides a useful first-order estimate, but full-wave simulation is required for precise characterization.

From a modeling perspective, the observed agreement validates the use of the ABCD-based code as a surrogate model for design and optimization. It is sufficiently accurate to guide the inverse design process and predict key performance metrics such as cutoff frequency, rejection depth, and bandwidth. At the same time, the differences observed in HFSS emphasize that the analytical

model should not be used as a final validation tool. Instead, it serves as an intermediate step that significantly reduces computational cost while preserving the essential physics of the system.

Overall, the results confirm that the implemented code faithfully reproduces the behavior reported in Ali Dehghanian's work [15]. The ABCD matrix model provides a reliable and efficient approximation of THz filter performance, while HFSS simulations capture the full electromagnetic complexity of the structure. The combination of both approaches offers a balanced framework in which rapid analytical design is complemented by high-fidelity numerical validation.

5. Conclusion and future work

5.1. Conclusion

This project successfully demonstrated the inverse design and validation of a planar low-pass terahertz (THz) filter using a Genetic-Algorithm–based optimization framework combined with ABCD matrix analysis and full-wave simulation in ANSYS HFSS. The automated workflow efficiently explored the binary design space of metallic and dielectric pixels, identifying non-intuitive geometries that satisfied the required low-pass characteristics while maintaining lithographic feasibility. In Chapter 2, the theoretical foundation of inverse design for electromagnetic structures was established. The discussion outlined the limitations of traditional forward design methods and demonstrated how inverse design—supported by analytical models such as the ABCD matrix—can overcome these constraints by directly mapping target frequency responses to optimized geometries. The methodology was further refined through the introduction of the genetic algorithm (GA), which provides robust global search capability in non-convex and high-dimensional design spaces. In Chapter 3, the final optimized design achieved a 3 dB cutoff frequency near 0.6 THz, an in-band insertion loss below 1.5 dB, and stopband suppression beyond −40 dB. The nearly linear phase progression across the passband confirmed low-dispersion transmission, which is essential for THz communication, imaging, and sensing applications.

The comparison between ABCD-based predictions and HFSS full-wave simulations showed close agreement in both magnitude and phase of the scattering parameters. Minor deviations at higher frequencies were primarily due to material dispersion and fringing effects not captured in the analytical model. This validation confirmed the accuracy and practicality of the GA–ABCD hybrid method for rapid THz filter design.

One important observation from this validation is that higher-frequency designs required minor parameter tuning within the implementation. This behavior is expected, as electromagnetic responses at higher frequencies become increasingly sensitive to geometric resolution and discretization effects.

Rather than indicating a limitation of the framework, these adjustments highlight the importance of scaling considerations in inverse electromagnetic design. The ability to maintain convergence with only small parameter changes demonstrates the flexibility of the GA–ABCD approach. The underlying optimization structure remained unchanged, confirming that the framework is robust while still allowing controlled adaptation to different operating regimes.

Overall, the developed framework proved that analytical-driven optimization can drastically reduce computation time while preserving physical accuracy. It provides a flexible and scalable foundation for designing other THz components such as band-stop, band-pass, and high-pass filters.

5.2. Future work

Although this project focused mainly on computational modeling and validation, several important directions remain for future development. The next major step is the experimental fabrication and testing of the GA-optimized coplanar stripline (CPS) filters. In future work, the optimized structures could be fabricated on a 1 μm silicon-nitride (Si_3N_4) membrane substrate using standard ultraviolet (UV) lithography and electron-beam physical vapor deposition. A gold layer, approximately 200 nm thick, could be deposited on a thin titanium adhesion layer to reproduce the electrical properties assumed in the simulations.

After fabrication, the device could be integrated with photoconductive switch (PCS) antennas to enable on-chip terahertz generation and detection. The experimental response could then be measured using a terahertz time-domain spectroscopy (THz-TDS) system. In this setup, femtosecond laser pulses would excite the transmitter PCS and generate broadband THz radiation, which would propagate through the optimized CPS filter. The transmitted signal would be detected by a second PCS, and the measured time-domain waveform could be converted into the frequency domain using a Fourier transform. This would allow the experimental S-parameters to be extracted and directly compared with both the ABCD-matrix predictions and the HFSS full-wave simulations.

This experimental comparison would be an important step in evaluating the reliability of the inverse-design framework. If the measured cutoff frequencies, notch frequencies, bandwidths,

and rejection levels agree well with the simulation results, it would confirm the predictive accuracy of the GA–ABCD–HFSS design approach. However, any differences between the measured and simulated responses would also provide valuable information. These deviations could be analyzed in terms of fabrication tolerances, finite conductor losses, radiation effects, surface roughness, and other physical effects that are not fully captured by the idealized analytical model.

Another important direction for future work is to perform a sensitivity, or robustness, analysis of the optimized filter geometries. The designs presented in this project are based on ideal structures generated by the optimization code and validated in HFSS. In a real fabricated device, however, the final geometry may not exactly match the simulated design. Small manufacturing defects, such as variations in conductor width, gap spacing, metal thickness, substrate thickness, edge roughness, alignment errors, or local defects in the gold pattern, can affect the electromagnetic response of the filter. These variations may change the scattering parameters, especially $S_{21}$and S_{11}, and may shift the cutoff frequency, notch frequency, rejection depth, insertion loss, or impedance matching behavior.

A future robustness study could investigate these effects by introducing controlled perturbations into the optimized geometries and recalculating the S-parameters using both the ABCD model and HFSS. For example, the conductor width and spacing could be increased or decreased by a fixed percentage, random edge roughness could be added to the metallic boundaries, or selected pixels could be modified to represent lithography defects. By comparing the perturbed and unperturbed responses, it would be possible to determine which geometric parameters have the strongest influence on filter performance.

This type of analysis would be especially useful for the band-stop filters, because their response depends on localized resonant behavior. Small fabrication errors may shift the notch frequency or reduce the rejection depth more strongly than in low-pass filters, which are governed by a more distributed impedance transition. Therefore, comparing the sensitivity of low-pass and band-stop designs would help identify which filter types are more tolerant to manufacturing imperfections and which require tighter fabrication control.

Future work could also extend the developed THz Inverse Design Configuration and Launcher program by comparing different optimization methods. Although this project used the genetic algorithm, the same framework can be expanded to evaluate other methods, such as Particle Swarm Optimization (PSO) and the Adjoint Method. These approaches could be compared in terms of convergence speed, computational efficiency, final fitness value, and sensitivity to design constraints. Such a comparison would help determine which optimization strategy is most suitable for different types of THz filter design.

In addition, the framework could be extended toward reconfigurable and multiband THz filters. This could be achieved by introducing tunable materials or variable geometries, such as MEMS-controlled gaps, graphene layers, or varactor-based impedance elements. These additions could allow dynamic tuning of the center frequency, bandwidth, or rejection level. Multi-objective optimization could also be included to design filters with more than one operating band or with improved phase characteristics for communication and spectroscopy applications.

Overall, future work should move the framework from ideal simulation toward fabrication-aware design. The sensitivity analysis would be particularly important because it would show how realistic manufacturing defects affect the S-parameters and overall filter behavior. By identifying the most critical geometric parameters, future versions of the optimization code could include fabrication tolerances directly in the fitness function. This would allow the algorithm to search not only for high-performance filters, but also for designs that remain stable and reliable under realistic manufacturing conditions. In this way, the GA–ABCD–HFSS framework could become a stronger foundation for practical, compact, and fabrication-ready THz components for communication, imaging, and spectroscopy applications.

References

[1] M. Tonouchi, “Cutting-edge terahertz technology,” *Nature Photonics*, vol. 1, pp. 97–105, 2007.

[2] J. Federici and L. Moeller, “Review of terahertz and sub-terahertz imaging,” *Journal of Applied Physics*, vol. 107, 043103, 2010.

[3] Y. Lee, Principles of Terahertz Science and Technology. Boston, MA: Springer US, 2009. doi: 10.1007/978-0-387-09540-0.

[4] P. U. Jepsen, D. G. Cooke, and M. Koch, “Terahertz spectroscopy and imaging—Modern techniques and applications,” *Laser & Photonics Reviews*, vol. 5, no. 1, pp. 124–166, 2011.

[5] K. Peiponen, J. Zeitler, and M. Kuwata-Gonokami, *Terahertz Spectroscopy and Imaging*, Springer, 2013.

[6] X. Yang et al., “Biomedical applications of terahertz spectroscopy and imaging,” *Trends in Biotechnology*, vol. 34, no. 10, pp. 810–824, 2016.

[7] D. H. Auston, “Picosecond optoelectronic switching and gating in GaAs,” Applied Physics Letters, vol. 26, pp. 101–103, 1975.

[8] H. T. Chen et al., “Active terahertz metamaterial devices,” *Nature*, vol. 444, pp. 597–600, 2006.

[9] T. Kleine-Ostmann and T. Nagatsuma, “A review on terahertz communications research,” *Journal of Infrared, Millimeter, and Terahertz Waves*, vol. 32, pp. 143–171, 2011.

[10] K. Tekbiyik et al., “Terahertz band communication: The last piece of spectrum puzzle for 6G,” *IEEE Open Journal of the Communications Society*, vol. 3, pp. 1–27, 2022.

[11] D. M. Pozar, *Microwave Engineering*, 4th ed., Wiley, 2012.

[12] S. Asadi, *Design and Testing of a Terahertz Bandstop Filter Using Varying Radii Split-Ring Resonators*, MASc Thesis, University of Victoria, 2024.

[13] C. Caloz and T. Itoh, *Electromagnetic Metamaterials: Transmission Line Theory and Microwave Applications*, Wiley, 2006.

[14] R. E. Collin, *Foundations for Microwave Engineering*, 2nd ed., McGraw-Hill, 1992.

[15] S. Dehghanian, *Genetic Algorithm Optimization of THz Coplanar Stripline Filters*, PhD Thesis, University of Victoria, 2025.

[16] H. Song and T. Nagatsuma, "Present and future of terahertz communications," *IEEE Trans. Terahertz Science and Technology*, vol. 1, no. 1, pp. 256–263, 2011.

[17] F. E. Terman, *Radio Engineers' Handbook*, McGraw-Hill, 1943.

[18] R. Marqués et al., "Role of losses in metamaterial transmission lines," *Physical Review B*, vol. 65, 144440, 2002.

[19] D. Grischkowsky et al., "Far-infrared time-domain spectroscopy with terahertz beams," *J. Opt. Soc. Am. B*, vol. 7, pp. 2006–2015, 1990.

[20] H. Smith and T. Darcie, "Dispersion control in coplanar THz lines," *Applied Physics Letters*, vol. 115, 2019.

[21] N. Engheta and R. W. Ziolkowski, *Metamaterials: Physics and Engineering Explorations*, Wiley-IEEE Press, 2006.

[22] H. L. Van Trees, *Detection, Estimation, and Modulation Theory*, Wiley, 2001.

[23] P. U. Jepsen and B. M. Fischer, "Dynamic range in terahertz time-domain spectroscopy," *Optics Letters*, vol. 30, pp. 29–31, 2005.

[24] M. D. Llorens et al., "Bloch impedance and dispersion in periodic CPW structures," IEEE Trans. Microwave Theory Tech., vol. 54, no. 12, pp. 4502–4511, 2006.

[25] A. Piggott et al., "Inverse design and implementation of a wavelength demultiplexing grating coupler," *Nature Photonics*, vol. 9, pp. 374–377, 2015.

[26] M. Molesky et al., "Inverse design in nanophotonics," *Nature Photonics*, vol. 12, pp. 659–670, 2018.

[27] J. Lu and J. Vučković, "Objective-first design of high-efficiency, small-footprint couplers between arbitrary nanophotonic waveguide modes," *Optics Express*, vol. 20, pp. 7221–7236, 2012.

[28] J. H. Holland, *Adaptation in Natural and Artificial Systems*, University of Michigan Press, 1975.

[29] S. Dehghanian, et al. "Demonstration of a planar multimodal periodic filter at THz frequencies." *Journal of Infrared, Millimeter, and Terahertz Waves* 46, no. 6: 37, 2025.

[30] S. Lucyszyn, “Investigation of anomalous room-temperature conduction losses in metals at THz frequencies,” *IEE Proc. Microwaves Antennas Propag.*, vol. 151, no. 4, pp. 321–329, 2004.

[31] Ghione, G., & Naldi, C. (1984). Analytical formulas for coplanar lines in hybrid and monolithic MICs. *Electronics Letters, 20*(4), 179–181.

[32] A. Dehghanian, T. Darcie, and L. Smith, “Genetic Algorithm-Based Inverse Design of Guided Wave Planar Terahertz Filters,” *arXiv preprint* arXiv:2506.03372 (2025).

[33] Z. Michalewicz, *Genetic Algorithms + Data Structures = Evolution Programs*, 3rd ed., Springer-Verlag, 1996.

[34] D. E. Goldberg and K. Deb, “A Comparative Analysis of Selection Schemes Used in Genetic Algorithms,” *Foundations of Genetic Algorithms*, pp. 69–93, 1991.

[35] https://github.com/Adehghanian/THz-Filter-Inverse-Design